INTERNATIONAL JOURNAL FOR NUMERICAL METHODS IN ENGINEERING

Int. J. Numer. Meth. Engng 2009; **00**:1 *Prepared using* nmeauth.cls *[Version: 2002/09/18 v2.02]*

A fracture framework for Euler Bernoulli beams based on a full discontinuous Galerkin formulation/extrinsic cohesive law combination

G. Becker[†], L. Noels[‡,*]

University of Liège, Computational & Multiscale Mechanics of Materials,

Chemin des Chevreuils 1, B-4000 Liège, Belgium

SUMMARY

A new full Discontinuous Galerkin discretization of Euler Bernoulli beam is presented. The main interest of this framework is its ability to simulate fracture problems by inserting a cohesive zone model in the formulation. With a classical Continuous Galerkin method the use of the cohesive zone model is difficult because as insert a cohesive element between bulk elements is not straightforward. On one hand if the cohesive element is inserted at the beginning of the simulation there is a modification of the structure stiffness and on the other hand inserting the cohesive element during the simulation requires modification of the mesh during computation. These drawbacks are avoided with the presented formulation as the structure is discretized in a stable and consistent way with full discontinuous elements and inserting cohesive elements during the simulation becomes straightforward. A new cohesive law based on the resultant stresses (bending moment and membrane) of the thin structure

*Correspondence to: L.Noels@ulg.ac.be

[†]PhD candidate at the Belgian National Fund for Education at the Research in Industry and Farming

[‡]University of Liége, department of Aerospace and Mechanical Engineering Department, CM3.

Received

Revised

discretization is also presented. This model allows propagating fracture while avoiding through-the-thickness integration of the cohesive law. Tests are performed to show that the proposed model releases, during the fracture process, an energy quantity equal to the fracture energy for any combination of tension-bending loadings.

KEY WORDS: Euler Bernoulli beam; discontinuous Galerkin method; fracture; finite-element; cohesive model

1. INTRODUCTION

When considering thin structures, tearing prediction remains challenging. This increases the interest of fracture and rupture numerical models for thin bodies, which must be able to take into account a through-the-thickness fracture.

A common approach in fracture mechanics is the cohesive zone concept pioneered by Dugdale [1] and Barenblatt [2]. This approach considers a tension between crack faces in the zone ahead of the crack tip. This tension is modeled by a "Traction Separation Law" (TSL) which gives a relationship between the tension and the opening of the crack faces (Δ). For Dugdale's model, developed for thin perfectly plastic steel sheets, tension is constant with Δ and corresponds to the yield stress, while for Barenblatt's model, developed for brittle materials, this tension represents the atomic cohesion and so decreases with the opening Δ.

In Finite Element (FE) methods this cohesive zone concept can be combined with cohesive elements [3–10], which are interface elements inserted between bulk elements. There are two ways of inserting these cohesive elements. On one hand the cohesive elements can be inserted at the beginning of the computation [4,6,9,11], in which case the cohesive elements must consider

the stage of pre-fracture and the cohesive law is called intrinsic. This pre-fracture behavior is achieved by introducing an initial slope in the TSL (see figure 1), and in order to have a correct wave propagation this slope must tend to infinity which leads to an ill-conditioned stiffness matrix or to a time step tending toward zero for explicit resolution schemes [12]. This problem limits the applicability of the intrinsic approach to cases where the crack path is known in advance which allows to insert cohesive elements only in well defined zones or to cases where a physical interpretation can be given to the slope of TSL (e.g. fiber coating, adhesive layers,...). On the other hand the cohesive elements can be inserted on the fly during the simulation when a criterion of crack initialization is reached [3, 7, 8, 10]. In this approach the cohesive element does not consider the phase of pre-fracture so the cohesive law is said to be extrinsic. During the pre-fracture stage, there is no modification of stiffness and so no alteration of the wave propagation. However the insertion of the cohesive elements during the simulation is very complex due to the dynamic modification of the mesh topology. Moreover the cohesive methods require a large number of elements in order to achieve convergence [7], requiring a large number of nodes. Therefore the use of a parallel code becomes mandatory, which complicates the dynamic modification of the mesh.

Insertion of cohesive elements with an extrinsic approach in a efficient way requires the use of complex topological data structure [13, 14] or topological graphs [15]. It was shown that such implementation could result in efficient 2D [14] or 3D [15] simulations. However the extension of such methods to parallel simulations has still yet to be proved. The main problem in the extension to the parallel case lies in the inherent difficulty associated with propagating topological changes in the mesh across processor boundaries. A way of avoiding these issues is presented by I. Dooley *et. al.* in [16] where their formulation is based on dormant nodes

concept. Another method combining advantages of both extrinsic and intrinsic approaches has been developed by Y. Monerie and F. Perales [17, 18]. It is based on inserting interface elements from the beginning but compatibility is enforced by Lagrangian multipliers, which, in turns, introduces new unknowns. An alternative approach avoiding to resort to new degrees of freedom is the recourse to Discontinuous Galerkin (DG) method.

DG is now commonly used to solve hyperbolic problems [19] and, more recently, has been used to solve elliptic problems [20–35]. This method allows to enforce weakly the compatibility condition through element boundary integral terms, and since the interface elements are naturally present, they can be directly used to model fracture. This approach has been pioneered by J. Mergheim *et al.* [36] and by A. Seagraves *et al* [37, 38]. This method is scalable when parallelized [37] and, as it will be shown, it does not require the use of complex topological information and can be implemented easily into existing FE codes. In this paper this framework is extended to thin structures, and more particularly to beams. For completeness, let us note that combination of cohesive law and discontinuous Galerkin method can also be achieved using a space-time discontinuous method [39]. This method allows controlling spatial and temporal resolutions and has been successfully implemented for 2D spatial problems with predefined cohesive surfaces [39].

Discontinuous Galerkin methods can also be applied to enforce weakly the C^1 continuity required by high-order formulations, which leads to displacement-field only methods (nodes have no degree of freedom of rotation). This method can be applied advantageously to beam, plate and shell problems where the C^1 continuity must be guaranteed [21, 29, 33, 34, 40]. In these works only C^1 is enforced by recourse to the DG method while the displacement field is continuous. By inserting discontinuous test functions and interface elements in such

formulations a new full-DG formulation is obtained and the study of its numerical properties shows that it is consistent, stable (if stabilization parameters are larger than mesh-independent constants) and converges in the $\mathbf{L}^2$ norm with the optimum rate. Afterward, this formulation can be used to solve fracture problems, as extrinsic cohesive law can easily be combined to the method. In this paper, such a displacement-field approach is developed for beams.

In discretization of thin structures with beam (plate or shell) elements, thickness is modeled implicitly as mesh discretization is in the plane of the structure only. This induces some difficulties for considering cohesive-separation laws for a bending problems where a part of the thickness is in compression and the other part is in tension. F. Cirak *et al.* suggested in [6] to use numerical integration on the thickness to take into account the stress field distribution on the thickness, but this requires to recompute the position of the neutral axis during the fracture process, which is not always numerically efficient. Therefore a new model is presented, which applies the cohesive principles directly to the resultant stresses (bending and membrane) in terms of the resultant openings (angle and mid-plane opening). This is based on the physics of fracture phenomena which require loadings to decrease with the increase of the crack length on the thickness. The new traction separation law is defined in such a way that the model respects the energetic balance during the fracture process for any coupled bending-traction loadings.

The article is organized as follows, first the governing equations of beams are summarized in section 2. Afterward, in section 3, these equations are discretized with a new full-DG formulation. Thereafter, the numerical properties of this new method are studied in an analytic way and illustrated by numerical examples. In section 4, a new cohesive zone model based on the resultant stresses is presented and then coupled with the full-DG formulation to take into

account brittle fracture. This section finishes with numerical applications of fracture testing to show the ability of the presented framework to simulate fracture problems. Finally some concluding remarks are drawn.

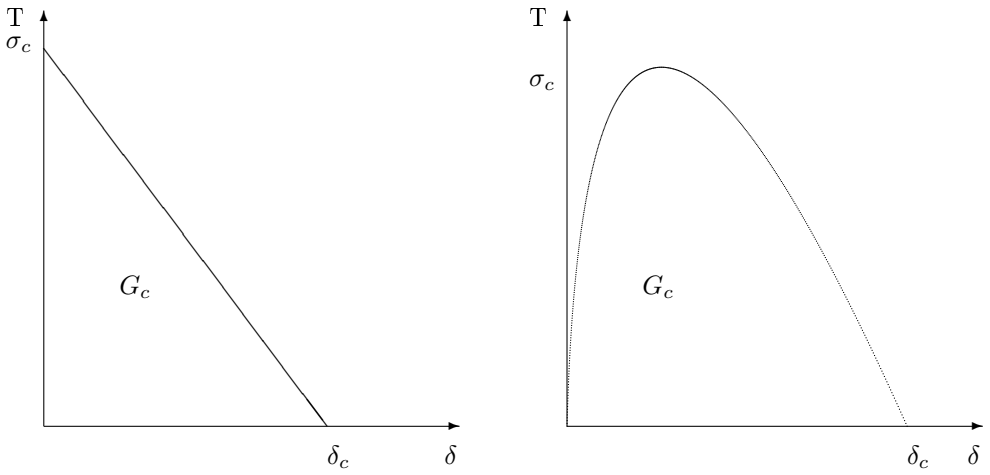

(a) (b)

Figure 1. Linearly decreasing monotonic (a) extrinsic and (b) intrinsic "Traction Separation Law"

2. CONTINUUM MECHANICS OF THIN BODIES: GOVERNING EQUATIONS OF BEAMS

For simplicity the following developments are made under the assumption of linear elasticity. The theory is based on the equations of linear momentum equilibrium,

$$\nabla \cdot \boldsymbol{\sigma} = 0 \text{ in } \mathcal{C} \tag{1}$$

and angular momentum equilibrium,

$$\mathbf{\Phi} \wedge \nabla \cdot \boldsymbol{\sigma} = 0 \text{ in } \mathcal{C} \tag{2}$$

where, in the two equations, the body forces $\boldsymbol{B}$ are assumed to be equal to zero for simplicity, $\boldsymbol{\sigma}$ is the Cauchy stress tensor, and where $\mathcal{C}$ represents a configuration of the thin body. In this last equation $\mathbf{\Phi}$ is the mapping of the thin body, which can be written in the particular case of linear Euler Bernoulli beam[†] as,

$$\mathbf{\Phi} = \mathbf{\Phi}_0 + u_1(\xi^1)\boldsymbol{E}_1 + u_3(\xi^1)\boldsymbol{E}_3 + \xi^3\left(\boldsymbol{E}_3 - u_{3,1}\boldsymbol{E}_1\right) \tag{3}$$

where $\mathbf{\Phi}_0$ represents the mapping between the configuration of reference and the initial configuration, u_i is the displacement in the direction of i axis, $\boldsymbol{E}_i$ are the unitary vectors of the inertial basis, ξ^1 is the curvilinear coordinate along the beam, and ξ^3 is the curvilinear coordinate over the thickness, which varies between h_{min} and h_{max} (of the undeformed beam) and is equal to zero on the neutral axis.

Using Simo [41, 42] developments in the particular case of the mapping $\mathbf{\Phi}$ (3) the two equations (1) and (2) can be rewritten [‡] in making by simplicity the assumption that there is no force exerted on the top and bottom surfaces of the beam, as

$$\left(\boldsymbol{n}^1\right)_{,1} = 0 \tag{4}$$

$$\left(\tilde{\boldsymbol{m}}^1\right)_{,1} - \boldsymbol{n}^3 = 0 \tag{5}$$

where the notations $\bullet_{,i}$ is used to refer to the derivative of $\bullet$ with respect to the curvilinear

[†]In this formulation the shearing is neglected, and the cross sections remain always perpendicular to the neutral axis, which leads to the expression of mid surface's direction for straight beams: $(\boldsymbol{E}_3 - u_{3,1}\boldsymbol{E}_1)$ used in equation (3)

[‡]For more details see [33]

coordinate i. and,

$$\boldsymbol{n}^1 = \int_{h_{min}}^{h_{max}} \boldsymbol{\sigma} \cdot \boldsymbol{E}_1 d\xi^3 \tag{6}$$

$$\boldsymbol{n}^3 = \int_{h_{min}}^{h_{max}} \boldsymbol{\sigma} \cdot \boldsymbol{E}_3 d\xi^3 \tag{7}$$

$$\tilde{\boldsymbol{m}}^1 = \int_{h_{min}}^{h_{max}} \xi^3 \boldsymbol{\sigma} \cdot \boldsymbol{E}_1 d\xi^3 \tag{8}$$

Finally, using plane stress assumption for beams ($\sigma_{12} = \sigma_{21} = \sigma_{22} = \sigma_{23} = \sigma_{32} = \sigma_{33} = 0$), the strong form of the problem can be expressed by,

$$\begin{cases} n^{11}_{,1} = 0 \\ \tilde{m}^{11}_{,1} - n^{31} = 0 \end{cases} \tag{9}$$

where n^{11}, $\tilde{m}^{11}$ and n^{31} are the first component of vectors $\boldsymbol{n}^1$, $\tilde{\boldsymbol{m}}^1$ and $\boldsymbol{n}^3$ respectively. The others components of these vectors are equal to zero with regard to the plane stress assumption. Note that however the shearing component n^{31} is usually neglected for Kirchhoff-Love and Euler-Bernoulli problems, it is kept in the present work to develop a full-DG formulation. The shearing will be neglected only at the end of formulation.

In the particular case of linear elasticity, the values of n^{11}, $\tilde{m}^{11}$ and n^{31} can directly be computed from the deformation mapping,

$$n^{11} = \int_{h_{min}}^{h_{max}} \sigma_{11} d\xi^3 = \int_{h_{min}}^{h_{max}} \left(E(u_{1,1} - u_{3,11}\xi^3) \right) d\xi^3 = Eh u_{1,1} \tag{10}$$

$$\tilde{m}^{11} = \int_{h_{min}}^{h_{max}} \sigma_{11} \xi^3 d\xi^3 = \int_{h_{min}}^{h_{max}} \left(E(u_{1,1} - u_{3,11}\xi^3) \right) \xi^3 d\xi^3 = -\frac{Eh^3}{12} u_{3,11} \tag{11}$$

$$n^{31} = \int_{h_{min}}^{h_{max}} \sigma_{31} d\xi^3 = \int_{h_{min}}^{h_{max}} \left(\frac{E}{2(1+\nu)} (u_{3,1} + \overline{\theta}) \right) d\xi^3 = \frac{Eh}{2(1+\nu)} (u_{3,1} + \overline{\theta}) \tag{12}$$

where E and ν are the Young's modulus and the Poisson's coefficient respectively, where $u_{3,1}+\overline{\theta}$ is the angle between the normal of the neutral axis and the cross-section direction. The signs result from convention as a positive angle around $\boldsymbol{E}_2$ corresponds to a negative slope in O_{xz} plane. This angle is equal to zero in case of Euler Bernoulli assumption.

3. FULL DG FORMULATION OF LINEAR BEAMS

3.1. Weak form of the equations

In this section the full DG FE discretization of equations (9) is introduced for Euler Bernoulli beams. Afterwards, the numerical properties of the new presented method are studied and illustrated on a numerical example. In this example the full discontinuous Galerkin formulation is compared to the CG/DG formulation introduced by Engel *et al* in [40]. It is observed that the full DG formulation gives the same results as the CG/DG approach, and has the same advantages, i.e. one-field locking-free approach. Obviously the full DG approach has a meaning only to take into account a pre-fracture stage. For the particular case of beams in small deformations and linear elasticity, the weak form of the problem (9) corresponds to

$$\int_0^L \left[n^{11}_{,1} \delta u_1 + \tilde{m}^{11}_{,1} \delta(-u_{3,1}) - n^{31} \delta(-u_{3,1}) \right] dx = 0 \tag{13}$$

This equation can be integrated by parts on each element $l_e \equiv [l_n \; l_{n+1}]$ of the FE discretization,

$$\begin{aligned} &\sum_e \Bigg\{ \int_{l_e} \left[n^{11} \delta u_{1,1} + \tilde{m}^{11} \delta(-u_{3,11}) - n^{31}_{,1} \delta(-u_3) \right] dx \\ &- \left(n^{11} \delta u_1 \big]_{l_e} + \tilde{m}^{11} \delta(-u_{3,1}) \big]_{l_e} - n^{31} \delta(-u_3) \big]_{l_e} \right) \Bigg\} = 0 \end{aligned} \tag{14}$$

where an unusual integration by parts is made on $\delta(-u_{3,1})$ instead of n^{31} for the third term of (13). In the equation (14), the following terms $\sum_e n^{11} \delta u_1 \big]_{l_e}$, $\sum_e n^{31} \delta(-u_3) \big]_{l_e}$ and $\sum_e \tilde{m}^{11} \delta(-u_{3,1}) \big]_{l_e}$ are related to discontinuities in the polynomial approximation between 2 elements. For a continuous Galerkin formulation, the continuity of the test functions allows to simplify the two first terms as $\sum_e \bullet]_{l_e} = \bullet]_0^L = 0$, since the test functions or the strains are null in 0 and L (depending on the boundary conditions). For the DG formulation, the test functions are discontinuous and these two terms can be rewritten as a sum of jumps over the

interface elements[§] s,

$$\sum_e n^{11}\delta u_1\big]_{l_e} = -\sum_s \left[\!\left[n^{11}\delta u_1\right]\!\right]_s \tag{15}$$

$$\sum_e n^{31}\left(-\delta u_3\right)\big]_{l_e} = -\sum_s \left[\!\left[n^{31}\left(-\delta u_3\right)\right]\!\right]_s \tag{16}$$

with the jump operator $\left[\!\left[\bullet\right]\!\right]_i = \left[\bullet^+ - \bullet^-\right]_i$. The remaining third term is related to discontinuities in the displacement derivative which leads to,

$$\sum_e \tilde{m}^{11}\delta(-u_{3,1})\big]_{l_n}^{l_{n+1}} = -\sum_s \left[\!\left[\tilde{m}^{11}\delta(-u_{3,1})\right]\!\right]_s \tag{17}$$

In DG formulations these jumps are commonly replaced by fluxes, which must be consistent. The developments are exactly the same for the three jumps, so in the following, only the equation (15) is developed and the two others terms (16) and (17) can be derived in the same way. Using the mathematical identity $\left[\!\left[ab\right]\!\right] = \langle a\rangle \left[\!\left[b\right]\!\right] + \langle b\rangle \left[\!\left[a\right]\!\right]$, relation (15) is rewritten as,

$$\sum_s \left[\!\left[n^{11}\delta u_1\right]\!\right]_s = \sum_s \left[\left\langle n^{11}\right\rangle \left[\!\left[\delta u_1\right]\!\right] + \left[\!\left[n^{11}\right]\!\right] \left\langle \delta u_1\right\rangle\right]_s \tag{18}$$

with the mean operator $\langle\bullet\rangle = \frac{1}{2}\left(\bullet^+ + \bullet^-\right)$. As for the exact solution there is no jump in the stress tensor between two elements, the second term of (18) can be neglected without altering the consistency and the flux related to (15) becomes,

$$\left[\!\left[n^{11}\delta u_1\right]\!\right] \rightarrow \left\langle n^{11}\right\rangle \left[\!\left[\delta u_1\right]\!\right] \tag{19}$$

To guarantee the compatibility and symmetry of the formulation, an extra term is introduced: $\langle Eh\delta u_{1,1}\rangle \left[\!\left[u_1\right]\!\right]$. As the exact solution of the problem is continuous, this term does not modify the consistency of the problem. Finally, as it is well known that, for elliptic problems,

[§]The equation (15) is obtained as follow : $\sum_e n^{11}\delta u_1\big|_{l_e} = \sum_e n^+_{x,e} n^{11+}_e \delta u_1^+ + n^-_{x,e} n^{11-}_e \delta u_1^- = -\sum_s \left[\!\left[n^{11}\delta u_1\right]\!\right]_s$, as normals $n^+_{x,e} = -1$ and $n^-_{x,e} = 1$

such a formulation is unstable, the method is stabilized by introducing a quadratic term: $[\![u_1]\!] \left\langle \frac{\beta_2 Eh}{h_s} \right\rangle [\![\delta u_1]\!]$, where h_s is the characteristic dimension of the element and where β_2 is a constant sufficiently large to ensure the stability of the problem. Such an introduction of interior penalty term is usual for discontinuous Galerkin method applied to solid mechanics, [20, 22, 25, 26] among others, and allows ensuring stability. Although the DG method is now slightly dissipative, this does not impact on the numerical accuracy as the method remains consistent and converges toward the solution with an optimal rate, see section 3.2, contrarily to methods using only a penalty coefficient. This user's parameter β_2 is independent of the mesh and material properties and is without dimension. Following these developments, the mathematical fluxes related to the equations (15), (16) and (17) are,

$$\sum_e n^{11}\delta u_1\big]_{l_e} \to -\sum_s \left(\langle n^{11} \rangle [\![\delta u_1]\!] + \langle Eh\delta u_{1,1} \rangle [\![u_1]\!] + [\![u_1]\!] \left\langle \frac{\beta_2 Eh}{h_s} \right\rangle [\![\delta u_1]\!] \right)_s \tag{20}$$

$$\begin{aligned} \sum_e \tilde{m}^{11}\delta(-u_{3,1})\big]_{l_n}^{l_{n+1}} \to -\sum_s \Bigg(\langle \tilde{m}^{11} \rangle [\![\delta(-u_{3,1})]\!] + \left\langle \frac{Eh^3}{12}\delta(-u_{3,11}) \right\rangle [\![-u_{3,1}]\!] \\ + [\![-u_{3,1}]\!] \left\langle \tfrac{\beta_1 Eh^3}{12h_s} \right\rangle [\![\delta(-u_{3,1})]\!] \Bigg)_s \end{aligned} \tag{21}$$

$$\sum_e n^{31}\left(-\delta u_3\right)\big]_{l_e} \to -\sum_s \left([\![u_3]\!] \left\langle \frac{\beta_3 Eh}{2(1+\nu)h_s} \right\rangle [\![(-\delta u_3)]\!] \right)_s \tag{22}$$

as ($n^{31} = 0$) in the relation (22), which implies that only the stabilization term remains in this equation. Let us note that the asymmetry in signs of relation (22) results from definition (12). Finally, after introducing the expressions (20), (21) and (22) in (14) the weak discretized form

of the problem becomes,

$$\begin{aligned} a(\boldsymbol{u},\delta\boldsymbol{u}) &= \sum_e \int_{l_e} \left[n^{11}\delta u_{1,1} + \tilde{m}^{11}\delta(-u_{3,11}) \right] dx \\ &+ \sum_s \Big(\langle n^{11} \rangle [\![\delta u_1]\!] + \langle Eh\delta u_{1,1} \rangle [\![u_1]\!] + [\![u_1]\!] \left\langle \frac{\beta_2 Eh}{h_s} \right\rangle [\![\delta u_1]\!] \\ &+ \langle \tilde{m}^{11} \rangle [\![\delta(-u_{3,1})]\!] + \left\langle \tfrac{Eh^3}{12}\delta(-u_{3,11}) \right\rangle [\![-u_{3,1}]\!] \\ &+ [\![-u_{3,1}]\!] \left\langle \tfrac{\beta_1 Eh^3}{12h_s} \right\rangle [\![-\delta u_{3,1}]\!] + [\![u_3]\!] \left\langle \tfrac{\beta_3 Eh}{2(1+\nu)h_s} \right\rangle [\![\delta u_3]\!] \Big) = 0 \end{aligned} \tag{23}$$

The relation (23) shows that a DG framework can be easily integrated in a CG FE code. Indeed the integral part of (23) is exactly the same as the one of a CG formulation of the problem with, as differences, the computation of a sum on interface elements which can be easily added in the FE code. For more convenience of further explanations the relation (23) can be expressed on the form,

$$\text{Structural terms} + \text{DG terms} = 0 \tag{24}$$

with Structural terms and DG terms respectively the integral part and the interface sum part of (23).

Note that a Gauss' rule is used to compute the bulk elements. For non linear law, Simpson's rule can be used to integrate (6) - (8) on the thickness.

Furthermore, if continuous test functions are used for displacement (ie the elements are continuous), it leads to $[\![\delta u_1]\!] = [\![\delta u_3]\!] = 0$ and the equation (23) can be simplified as,

$$\begin{aligned} a(\boldsymbol{u},\delta\boldsymbol{u}) &= \sum_e \int_{l_e} \left[n^{11}\delta u_{1,1} + \tilde{m}^{11}\delta(-u_{3,11}) \right] dx \\ &+ \sum_s \left(\langle \tilde{m}^{11} \rangle [\![\delta(-u_{3,1})]\!] + \left\langle \frac{Eh^3}{12}\delta(-u_{3,11}) \right\rangle [\![-u_{3,1}]\!] \right) \\ &+ [\![-u_{3,1}]\!] \left\langle \tfrac{\beta_1 Eh^3}{12h_s} \right\rangle [\![-\delta u_{3,1}]\!] \Big) = 0 \end{aligned} \tag{25}$$

This last equation is identical to the previously CG/DG formulation defined by G. Engel *et al* in [40].

3.2. Numerical properties

In this section the numerical properties of the weak formulation (23) are studied. It is demonstrated that the framework satisfies two fundamental properties of a numerical method: consistency and stability. This last one is demonstrated if the parameters β_1 and β_2 are large enough, and if β_3 is non zero. The convergence rate of the method in the energy norm with respect to the mesh size is proved to be equal to $k-1$, with k the degree of the polynomial approximation. Finally, optimal-convergence rate in the $\boldsymbol{L}^2$-norm is demonstrated for at least cubic elements. Afterward, some numerical examples are presented to illustrate these properties.

3.2.1. Consistency To prove the consistency of the method, the exact solution $\boldsymbol{u}$ of the problem is considered. As this exact solution is $\mathcal{C}^2([0\ L])$, this implies $[\![u_1]\!] = [\![u_3]\!] = [\![u_{3,1}]\!] = 0$, and relation (23) becomes,

$$\begin{aligned}&\sum_n \int_{l_e} \left[n^{11}\delta u_{1,1} + \tilde{m}^{11}\delta(-u_{3,11})\right] dx \\ &+ \sum_s \left(\langle n^{11}\rangle [\![\delta u_1]\!] + \langle \tilde{m}^{11}\rangle [\![\delta(-u_{3,1})]\!]\right) = 0\end{aligned} \tag{26}$$

Integrating by part on each element, as n^{11} and $\tilde{m}^{11}$ of the exact solution are continuous, leads to

$$-\int_0^L n^{11}_{,1}\delta u_1 dx - \int_0^L \tilde{m}^{11}_{,1}(-\delta u_{3,1})dx = 0 \tag{27}$$

The arbitrary nature of the test functions leads to the two following equalities,

$$n^{11}_{,1} = 0 \text{ in } [0\ L] \tag{28}$$

$$\tilde{m}^{11}_{,1} = 0 \text{ in } [0\ L] \tag{29}$$

These two equations (28) and (29) correspond to the strong formulation of the problem expressed by the relations (9) where the shearing is neglected ($n^{31} = 0$). Thus the consistency of the method is demonstrated. This property implies that the exact solution $\boldsymbol{u}$ satisfies (23), which provides the orthogonality relation,

$$a(\boldsymbol{u_h} - \boldsymbol{u}, \delta\boldsymbol{u}) = a(\boldsymbol{u}_h, \delta\boldsymbol{u}) - a(\boldsymbol{u}, \delta\boldsymbol{u}) = 0 \tag{30}$$

where $\boldsymbol{u}_h$ is the FE solution.

3.2.2. Stability To study the stability and convergence rate of the framework, an energy norm has to be defined. If constrained displacements $\overline{\boldsymbol{u}}$ and directions of the mid-surface $\overline{\boldsymbol{t}}$ are assumed to be equal to 0 on boundaries then the following energy norm can be considered,

$$\begin{aligned} |||\boldsymbol{u}|||^2 \;=\; & \sum_e \left|\left| \sqrt{Eh}\, u_{1,1} \right|\right|^2_{\mathbf{L}^2(l_e)} + \sum_s \left|\left| \sqrt{\frac{\beta_2 Eh}{h_s}}\, [\![u_1]\!] \right|\right|^2_{\mathbf{L}^2(s)} \\ & + \sum_e \left|\left| \sqrt{\frac{Eh^3}{12}}(-u_{3,11}) \right|\right|^2_{\mathbf{L}^2(l_e)} + \sum_s \left|\left| \sqrt{\frac{\beta_1 Eh^3}{12h_s}}\, [\![(-u_{3,1})]\!] \right|\right|^2_{\mathbf{L}^2(s)} \\ & + \sum_s \left|\left| \sqrt{\frac{\beta_3 Eh}{2(1+\nu)h_s}}\, [\![u_3]\!] \right|\right|^2_{\mathbf{L}^2(s)} \end{aligned} \tag{31}$$

where,

$$\left|\left| \sqrt{\mathcal{H}} a \right|\right|^2_{\mathbf{L}^2(l_e)} = \int_{l_e} \mathcal{H} a^2 d\mathcal{A} \tag{32}$$

$$\sum_s \left|\left| \sqrt{\mathcal{H}}\, [\![a]\!] \right|\right|^2_{\mathbf{L}^2(s)} = \sum_e \frac{1}{2} \left|\left| \sqrt{\mathcal{H}}\, [\![a]\!] \right|\right|^2_{\mathbf{L}^2(\partial l_e)} \tag{33}$$

The expression (31) defines a norm as $|||\boldsymbol{u}||| = 0$ only for $\boldsymbol{u} = 0$ on $[0\ L]$. This is demonstrated in the following way : if $|||\boldsymbol{u}||| = 0$ then each term is equal to 0. So on each element the derivatives $u_{1,1}$ and $-u_{3,11}$ are also equal to zero which implies that u_1 and $u_{3,1}$ are constant on each element. Moreover, as jump are equal to zero on the interface, u_1, u_3 and $u_{3,1}$ are constant on $]0\ L[$. Finally, the boundary conditions $\overline{\boldsymbol{u}} = 0$ and $\overline{\boldsymbol{t}} = 0$ imply $u_1 = u_3 = u_{3,1} = 0$ on $[0\ L]$.

Now to demonstrate the stability of the framework an upper and a lower bound of the bilinear form are needed. These two bounds can be established by following the developments given in [33]. The full DG formulation presented in this work implies more DG interface terms but they can be treated exactly as in [33] and the interested reader can refer to it for more details. An upper bound of the bilinear can be found as,

$$|a(\boldsymbol{u},\delta\boldsymbol{u})| \leq C''^{k}(\beta_1,\beta_2)\,|||\boldsymbol{u}|||\,|||\delta\boldsymbol{u}||| \tag{34}$$

where $C''^{k}(\beta_1,\beta_2)$ is a number larger than $\max(4,(C_\alpha^k)^2/\beta_\alpha)$, where $C_\alpha^k > 0$ are constant depending only on the degree of polynomial. A lower bound of the bilinear form is given by,

$$\begin{aligned} a(\boldsymbol{u},\boldsymbol{u}) \;\geq\; & (1-\epsilon_1)\sum_e \left|\left|\sqrt{Eh}u_{1,1}\right|\right|^2_{\mathbf{L}^2(l_e)} + (1-\epsilon_2)\sum_e \left|\left|\sqrt{\frac{Eh^3}{12}}u_{3,11}\right|\right|^2_{\mathbf{L}^2(l_e)} \\ & + \left(1-\frac{2(C_2^k(\beta_2))^2}{\epsilon_1\beta_2}\right)\sum_e \left|\left|\sqrt{\frac{Eh\beta_2}{2h_s}}\,[\![u_1]\!]\right|\right|^2_{\mathbf{L}^2(\partial l_e)} \\ & + \left(1-\frac{2(C_1^k(\beta_1))^2}{\epsilon_2\beta_1}\right)\sum_e \left|\left|\sqrt{\frac{Eh^3\beta_1}{24h_s}}\,[\![u_{3,1}]\!]\right|\right|^2_{\mathbf{L}^2(\partial l_e)} \\ & + \sum_e \left|\left|\sqrt{\frac{\beta_3 Eh}{4(1+\nu)h_s}}\,[\![u_3]\!]\right|\right|^2_{\mathbf{L}^2(\partial l_e)} \end{aligned} \tag{35}$$

where ϵ_1 and ϵ_2 are constant larger than zero coming from the so-called ϵ-inequality $\forall\epsilon>0: |ab| \leq \frac{\epsilon}{2}a^2 + \frac{1}{2\epsilon}b^2$ or $\forall\epsilon>0: |ab| \leq \epsilon a^2 + \frac{1}{4\epsilon}b^2$.

Finally, the stability of the method is directly demonstrated by relation (35). Indeed by definition of the energetic norm (31),

$$\begin{aligned} |||\boldsymbol{u}|||^2 \;=\; & \sum_e \left|\left|\sqrt{Eh}u_{1,1}\right|\right|^2_{\mathbf{L}^2(l_e)} + \sum_e \left|\left|\sqrt{\frac{Eh^3}{12}}u_{3,11}\right|\right|^2_{\mathbf{L}^2(l_e)} + \frac{1}{2}\sum_e \left|\left|\sqrt{\frac{\beta_1 Eh^3}{12h_s}}\,[\![u_{3,1}]\!]\right|\right|^2_{\mathbf{L}^2(\partial l_e)} \\ & + \frac{1}{2}\sum_e \left|\left|\sqrt{\frac{\beta_2 Eh}{h_s}}\,[\![u_1]\!]\right|\right|^2_{\mathbf{L}^2(\partial l_e)} + \frac{1}{2}\sum_e \left|\left|\sqrt{\frac{\beta_3 Eh}{4(1+\nu)h_s}}\,[\![u_3]\!]\right|\right|^2_{\mathbf{L}^2(\partial l_e)} \end{aligned} \tag{36}$$

Comparing the right term of equation (36) to the right term of equation (35) leads to,

$$a(\boldsymbol{u}_h, \boldsymbol{u}_h) \geq C(\beta_1, \beta_2) \, |||\boldsymbol{u}_h||| \tag{37}$$

where $C(\beta_1, \beta_2) > 0$ as for given $0 < \epsilon_1 < 1$ and $0 < \epsilon_2 < 1$ there always exist $\beta_1 > \frac{2(C_1^k)^2}{\epsilon_1}$ and $\beta_2 > \frac{2(C_2^k)^2}{\epsilon_2}$. This shows that the stability of the method is conditioned by the constant β_1 and β_2 which must be large enough. Note that the equation (37) does not imply stability conditions on the parameter β_3 as long as $\beta_3 > 0$.

3.2.3. Convergence rate in the energy norm In the following the error between the FE solution and the polynomial interpolation of the exact solution is calculated to establish the convergence rate in the energy norm of the method. First some definitions and hypothesis are given. Consider $\boldsymbol{u}$ the exact solution of the problem and $\boldsymbol{u}^k$ its FE interpolation defined by $\int_0^L (\boldsymbol{u} - \boldsymbol{u}^k) \delta \boldsymbol{u} dl = 0$. Furthermore, the errors on exact solution and on its interpolation are respectively defined by $\boldsymbol{e} = \boldsymbol{u}_h - \boldsymbol{u}$ and $\boldsymbol{e}^k = \boldsymbol{u}_h - \boldsymbol{u}^k$.

The demonstration follows the same procedure as in [33] so only the final result is given here,

$$\left|||\boldsymbol{e}^k|||\right| \leq C(\beta_1, \beta_2, \beta_3) \sum_e h_s^{k-1} \left|\boldsymbol{u}\right|_{\mathbf{H}^{k+1}(l_e)} \tag{38}$$

the order of convergence is one order lower than the degree of polynomial approximation which is consistent with the presence of high-order derivatives in the governing equations (9).

3.2.4. Convergence in the $\mathbf{L}^2$ *norm* The convergence of the solution in the $\mathbf{L}^2$ norm is demonstrated under the two assumptions:

1. Proper elliptic regularity of the problem
2. Pure Dirichlet boundary conditions (ie $\overline{\boldsymbol{u}} = \overline{\boldsymbol{t}} = 0$ on $\partial([0 \; L])$)

As well as the convergence rate in the energy norm, the demonstration of the convergence in the $\mathbf{L}^2$ norm follows the method presented in [33] so only the final result is given here,

$$||\boldsymbol{e}||_{\mathbf{L}^2(l_e)} \leq \begin{cases} \sum_e C h_s^{k+1} |\boldsymbol{u}|_{\mathbf{H}^{k+1}(l_e)} \text{ if } k > 2 \\ \sum_e C h_s^2 |\boldsymbol{u}|_{\mathbf{H}^3(l_e)} \text{ if } k = 2 \end{cases} \tag{39}$$

where the case $k = 2$ is obtained by following the work of Wells *et al.* [29]. The relation (39) demonstrates that the method has an optimal convergence rate for at least cubic element.

3.3. Numerical example: Double clamped beam with uniformly distributed loading

The numerical properties demonstrated above are illustrated on a test case. It shows that the convergence of solution with respect to the mesh size is in accordance with the theory and that the results are as accurate as the ones obtained with CG/DG formulation previously developed by Engel *et. al.* [40].

The example consists of a double clamped beam (DCB), whose material and geometrical properties are given in Table I, submitted to a distributed force $p = 4$ $[kN/m]$ (see Figure 2). This force induces a displacement field described analytically by (see [43]),

$$u_3(x) = \frac{p x^2 (L-x)^2}{24EI} \tag{40}$$

This case is simulated with quadratic and cubic elements for different mesh sizes h_s =1/4, 1/6, 1/8, 1/10, 1/12, 1/14, 1/16, 1/32, 1/64, 1/128, 1/256 and different stabilization parameter values $\beta_1 = 5, 10, 100, 1e4, 1e6$, $\beta_3 = 100\beta_1$. The choice for β_3 is illustrated on figure 3a which shows the convergence with β_3 of the normalized deflection of the test case for $h_s = 1/64$, $\beta_1 = \beta_2 = 10$ and for two different beam's height of 10[mm] and 100[mm]. It appears that the curves are exactly the same but are scaled by a factor 100. Therefore, the convergence with

	DCB
material properties	
Young's modulus (E)	10 [GPa]
Poisson's coefficient (ν)	0.21 [-]
density (ρ)	10000 $[kg/m^3]$
geometrical properties	
length (L)	1000 [mm]
height (h)	10 [mm]

Table I. Material and geometrical properties used of the DCB

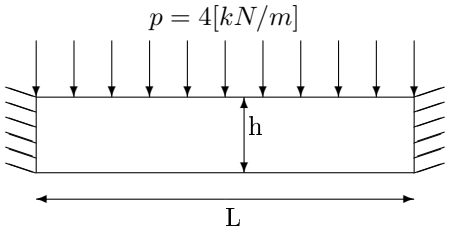

Figure 2. Double clamped beam in bending

β_3 depends on the geometry. To remove this dependency, β_3 has to be multiplied by a factor $(h/L)^2$. Indeed, when the height is divided by 10 the minimal β_3 which gives a converged solution is divided by 100. Furthermore, the same study can be realized on the beam's length

(3b), which shows than when L is divided by 10, the minimal β_3 which gives a converged solution is multiplied by 100. These results show that β_3 should be of the order of $\beta_1/(h/L)^2$ to be independent of the geometry. As in this test case the ratio $h/L = 1e-2$, β_3 is set to 100 times β_1 instead of 10000 in order to avoid ill conditioned matrix for large value of β_1. Note that as this test is in pure bending¶, there is no displacement along x ($u_1 = 0$) and the value of β_2 does not modify the results.

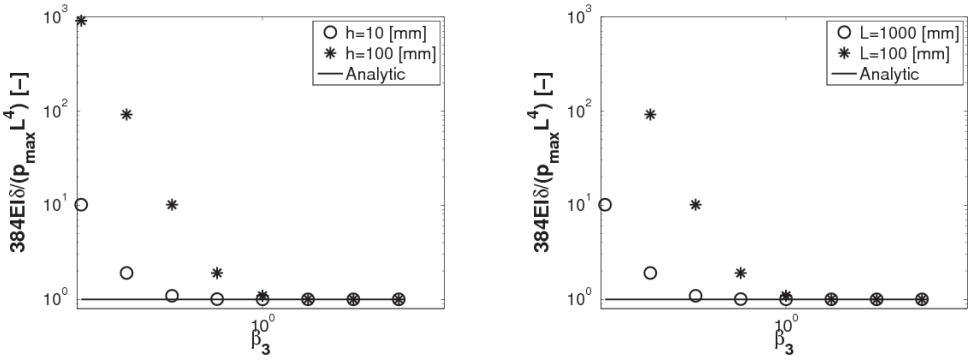

(a) (b)

Figure 3. Convergence of normalized deflection with respect to β_3 in function of geometrical parameters. (a) study on height and (b) study on length.

Figure 4 shows the normalized deformation for $\beta_1 = 100$. As the profile is well fitted with a mesh size of $h_s = 1/64$ the profile is not plotted for finer mesh sizes. So the convergence is achieved for respectively 100, 192, 128 and 168 degrees of freedom for quadratic CG/DG , quadratic full DG, cubic CG/DG and cubic full DG elements. The graphs are obtained with (a) quadratic elements and a CG/DG formulation, (b) quadratic elements and the full DG

¶As shearing is neglected in Euler Bernoulli beams

formulation, (c) cubic elements and a CG/DG formulation and (d) cubic elements and the full DG formulation. They show that the analytical solution is very well approximated for both degrees of elements and that the full DG formulation gives the same results as the CG/DG method.

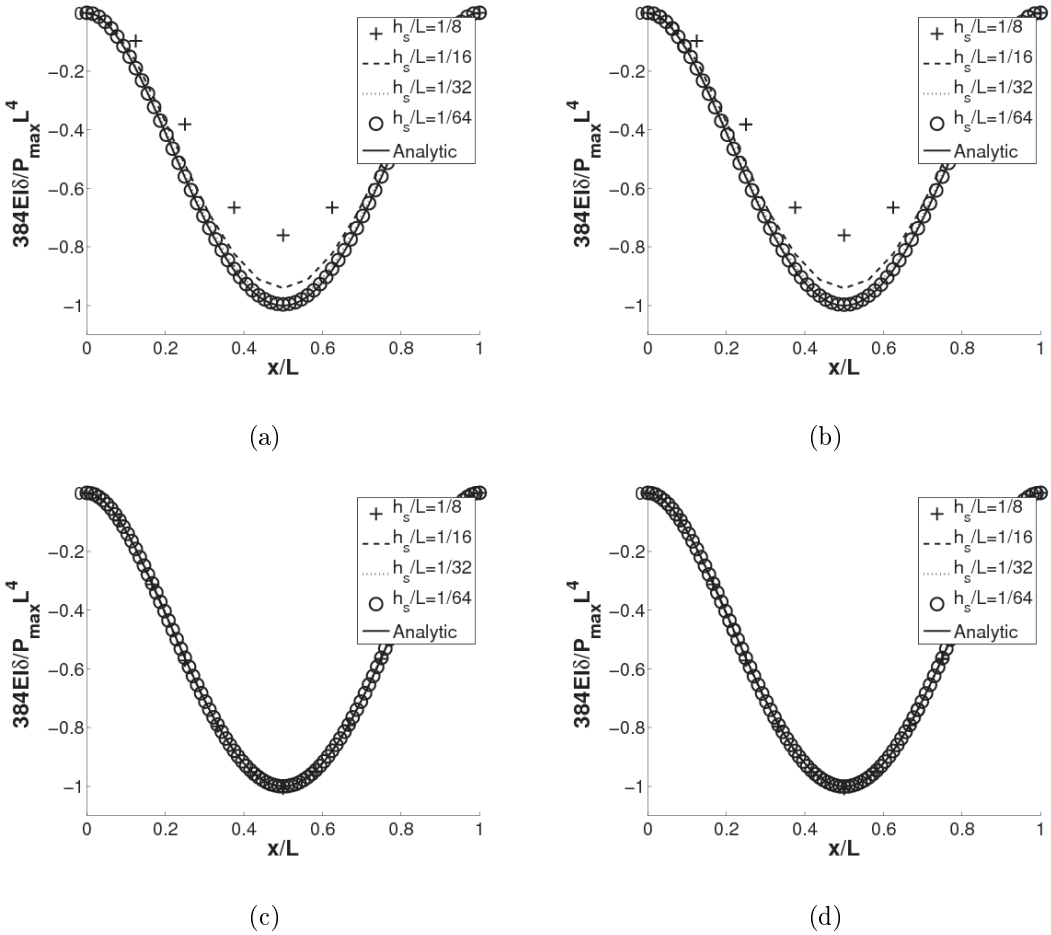

Figure 4. Deformation profile of DCB for (a) quadratic elements with CG/DG formulation, (b) quadratic elements with full DG formulation, (c) cubic elements with CG/DG formulation, (d) cubic elements with full DG formulation

Figure 5 plots the normalized maximal deflection of the beam for (a) quadratic elements with CG/DG formulation, (b) quadratic elements with full DG formulation, (c) cubic elements with CG/DG formulation and (d) cubic elements with full DG formulation. This figure shows that for any degree of elements and for $\beta_1 \geq 5$, both methods are stable. However for values of $\beta_1 > 1e6$ (quadratic elements) and $\beta_1 > 1000$ (cubic elements) both methods suffer from locking for the finer mesh, which leads to low convergence rate in the L^2 norms in these cases Finally this figure shows that the full DG method converges toward a less stiff solution for small values of β_1 ($\beta_1 \approx 10$) due to the weak enforcement of the compatibility. Nevertheless the error between analytic and the full DG solution with low β_1 value is approximately equal to 2% which is acceptable. From this example, it appears that as long as the stabilization parameter β_1 remains in the rather wide range [5-1000], numerical accuracy of the method is ensured. Same behavior was observed for different applications of discontinuous Galerkin methods for solids [25, 32, 33] and for shells, which allows to conclude that this range is non-dependent from the problem under consideration.

Figures 6 and 7 give the convergence rate in $\boldsymbol{L}^2$ and energetic norms respectively with respect to the mesh size, and for (a) quadratic elements and a CG/DG formulation, (b) quadratic elements and a full DG formulation, (c) cubic elements with a CG/DG formulation and (d) cubic elements with a full DG formulation. These figures show that both convergence rates correspond to those predicted by theory, unless locking or numerical accuracy for low errors prevent reaching this convergence rate. Moreover, the convergence in $\boldsymbol{L}^2$ norm is in $k+1$ even for quadratic elements where theory predicts a convergence only in k. This observation is in agreement with what show by L. Noels *et. al* in [33] and by G. Wells in [29] for C0/DG shells. One more time, the two figures show that the same results are obtained by CG/DG and full

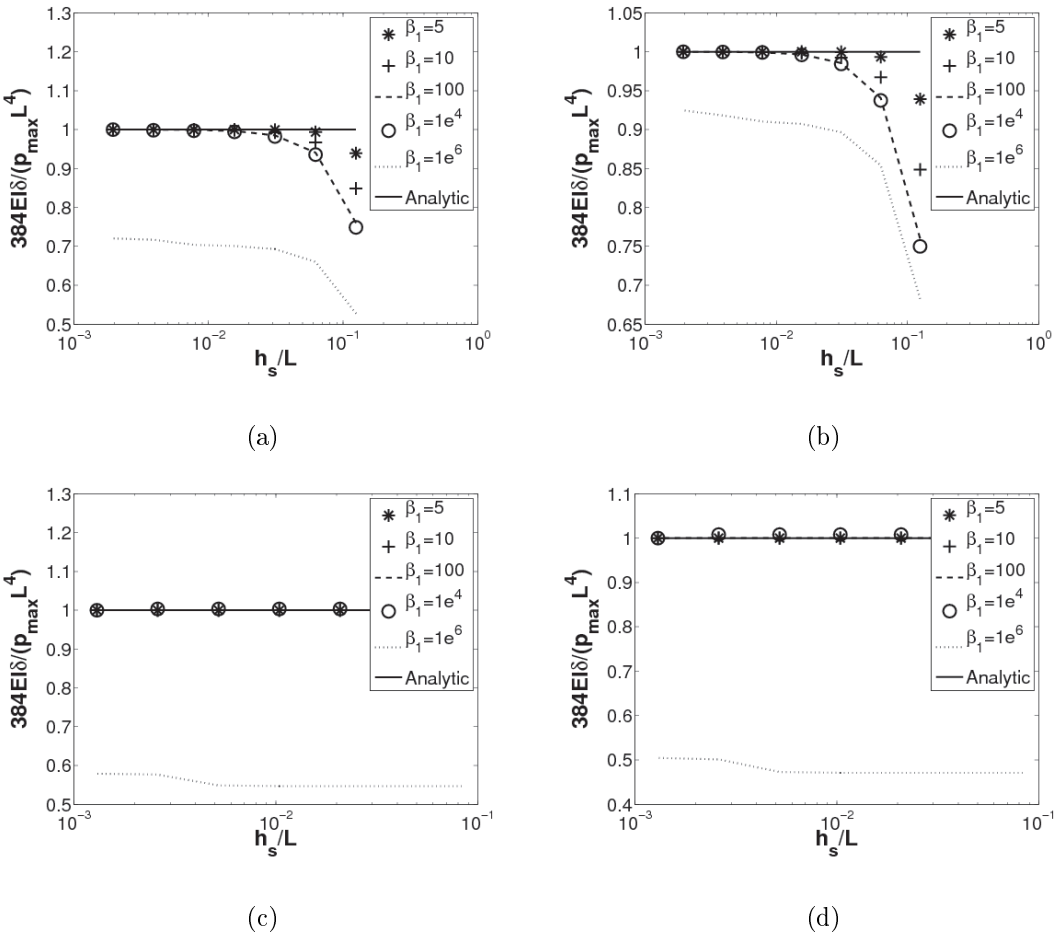

Figure 5. Maximal deflection convergence with respect to the mesh size for (a) quadratic elements with a CG/DG formulation, (b) quadratic elements with a full DG formulations, (c) cubic elements with a CG/DG formulation and (d) cubic elements with a full DG formulation

DG methods.

Finally, figure 8 illustrates the condition number of the stiffness matrix with respect of the number of elements for different values of parameters β_i ($\beta_2 = \beta_1$ and $\beta_3 = 100\beta_1$). The condition numbers depict on the figure are divided by the condition number of the elementary

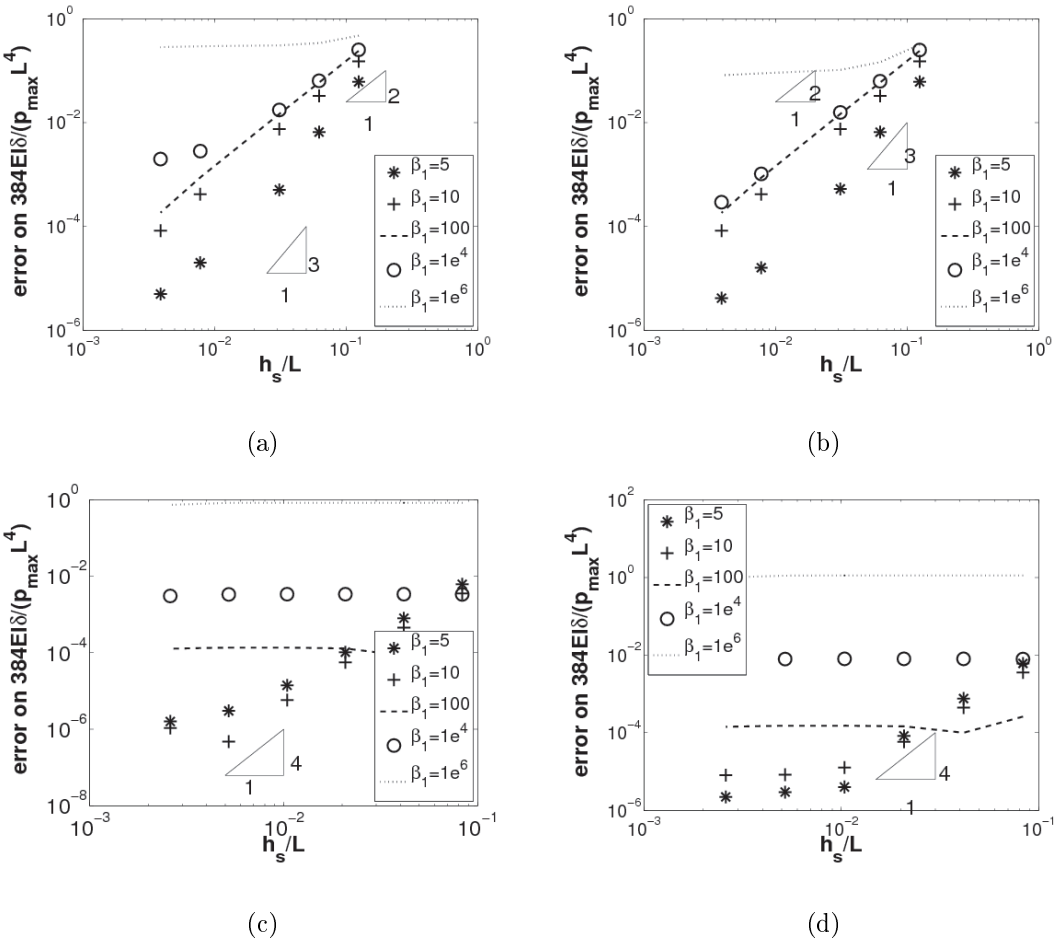

Figure 6. L^2 error convergence with respect to the mesh size for (a) quadratic elements with a CG/DG formulation, (b) quadratic elements with a full DG formulations, (c) cubic elements with a CG/DG formulation and (d) cubic elements with a full DG formulation

bulk matrix to be independent of material and geometry. Moreover, they are reported for both CG/DG (a) and (c) and full DG (b) and (d) formulations, as well as for elements of degree 2 (a) and (b) and elements of degree 3 (c) and (d). These graphs show that the condition number is approximately the same for the two formulations and the two degrees of element.

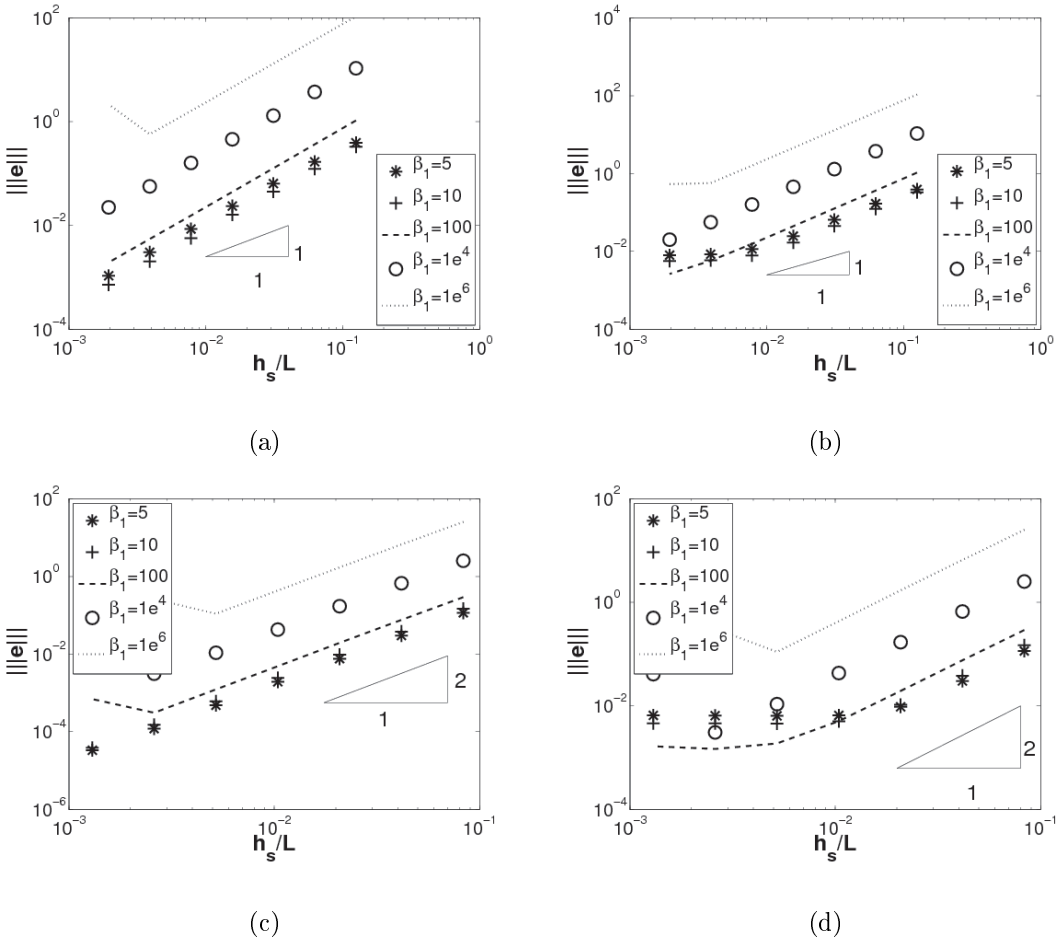

Figure 7. Error in energetic norm convergence with respect of the mesh size for (a) quadratic elements with a CG/DG formulation, (b) quadratic elements with a full DG formulations, (c) cubic elements with a CG/DG formulation and (d) cubic elements with a full DG formulation

Furthermore, for all the cases, the condition number increases with the fourth power of the number of elements and increases linearly with the parameter β_1. So for large stabilization parameters β_i, an ill-conditioned matrix is expected. However, in the practical range ($\beta_1 \simeq 10$), the condition numbers remain satisfactory.

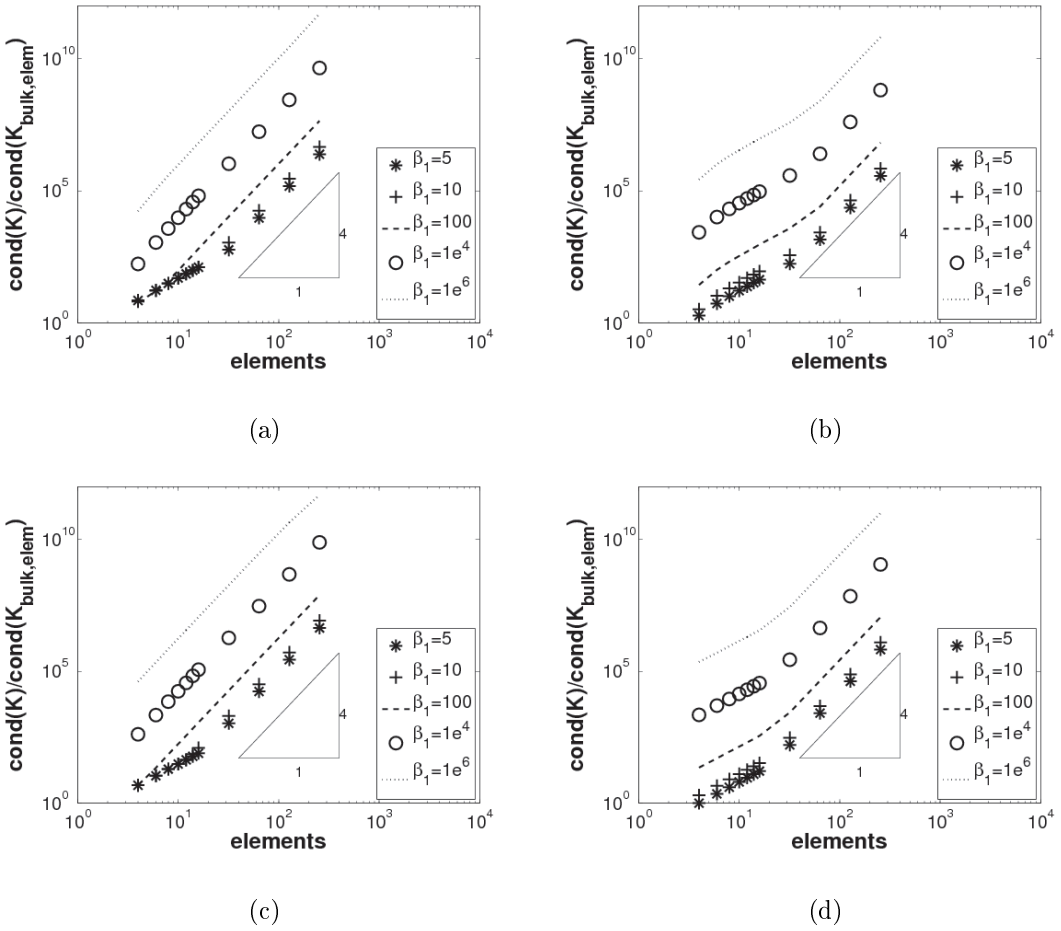

Figure 8. Condition number of the stiffness matrix with respect to the number of elements for (a) quadratic elements with a CG/DG formulation, (b) quadratic elements with a full DG formulations, (c) cubic elements with a CG/DG formulation, and (d) cubic elements with a full DG formulation

4. APPLICATION TO FRACTURE MECHANICS

4.1. DG/Extrinsic Cohesive Law combined method

In this section, a fracture model is coupled with the full-DG beam formulation introduced in section 3. The full-DG framework can be advantageously combined with an extrinsic cohesive

approach as the pre-fractured stage is modeled in a stable and consistent way (see section 3.2). As interface elements have already been introduced, it is not necessary to modify dynamically the mesh in order to introduce the cohesive elements, which is the critical step of classical extrinsic cohesive approaches. The cohesive elements "substitute" simply the interface elements where the fracture criterion is reached. Mathematically the equation (24) can be rewritten as introduced first by J. Mergheim *et al.* [36],

$$\text{Structural terms } + (1-\alpha) \text{ DG terms } + \alpha \text{ cohesive term } = 0 \tag{41}$$

where α is evaluated at each interface element and is equal to 1 if there is fracture and is equal to 0 if this is not the case. For Euler Bernoulli beams, only the normal stress component is different from zero and a fracture criterion in tension can be considered,

$$\max_{\xi^3} \left\langle \sigma^{11} \right\rangle - \sigma_c > 0 \tag{42}$$

where the operator $\langle \bullet \rangle$ represents the mean value on the interface element and where σ_c, the fracture strength, is a material parameter.

The cohesive zone concept, initially presented by Barenblatt [2], is based on the existence of a residual traction while crack faces are still in a close neighborhood. In this model of perfectly brittle fracture, the traction represents the physical inter-atomic attractive forces which are exerted between atoms. After a given distance Δ_c this traction falls to zero and there is no force exerted between crack faces. In more general cases, the traction-separation law represents physical phenomena happening in the process zone. The application of J-integral concept introduced by J.R. Rice [44] leads to the general form of cohesive term,

$$\delta J = \int \boldsymbol{T} \cdot \delta(\boldsymbol{\Delta}) dS \tag{43}$$

with $\boldsymbol{T}$ the traction forces exerted between crack faces and $\boldsymbol{\Delta}$ the opening between them. In the

article the normal to the fracture is equal to E_1 as the linear assumption is made[‖]. Therefore vectors $\boldsymbol{T}$ and $\delta(\boldsymbol{\Delta})$ have a non-zero component only along axis 1, which are respectively noted t and Δ in the following. Moreover, as the cohesive term (43) is equal to J-integral the area under the TSL must be equal to the energy of rupture G_c, a material parameter [45], if the crack grows straight ahead, which is the case in this paper. So the two parameters of the TSL are σ_c and G_c, the critical opening value Δ_c being deduced from the traction-separation law shape, see Fig. 1.

As the focus is put on thin bodies where the thickness is implicitly modeled, it is not straightforward to take into account a through the thickness fracture. A solution is suggested by F. Cirak *et al.* in [6], where the traction-separation-law is integrated at each Simpson points

[‖]The normal to the fracture $\boldsymbol{n}_s$ in the current configuration of the interface element can be computed as suggested by F. Cirak *et al.* in [6],

$$\boldsymbol{n}_s = \frac{\langle \boldsymbol{n}_s \rangle}{||\langle \boldsymbol{n}_s \rangle||}$$

with $\boldsymbol{n}_s^{\pm}$ equal to,

$$\boldsymbol{n}_s^{\pm} = \boldsymbol{\tau}^{\pm} \wedge \boldsymbol{t}^{\pm}$$

where $\boldsymbol{t}$ and $\boldsymbol{\tau}$ are respectively the normal of the neutral axis and the tangent vector at the interface element. For beam elements these quantities are equal to,

$$\boldsymbol{t} = \boldsymbol{E}_3 - u_{3,1}\boldsymbol{E}_1$$

$$\boldsymbol{\tau} = \boldsymbol{E}_2$$

which leads to,

$$\boldsymbol{n}_s = \frac{\boldsymbol{E}_1 + \langle u_{3,1} \rangle \boldsymbol{E}_3}{\sqrt{1 + \langle u_{3,1} \rangle^2}} \approx \boldsymbol{E}_1$$

describing the thickness. As the TSL makes sense only for traction, this solution is difficult to implement and another approach considering a traction-separation law based on the resultant stresses is suggested. The cohesive integral (43) is replaced by the application of cohesive law on the resultant membrane $\langle n^{11} \rangle$ and bending $\langle m^{11} \rangle$ stresses, which are denoted N and M respectively after fracture is initiated, leading to,

$$\boldsymbol{T} \cdot \delta(\boldsymbol{\Delta}) dS \rightarrow N(\Delta^*)\delta([\![u_1]\!]) + M(\Delta^*)\delta([\![-u_{3,1}]\!]) \tag{44}$$

where Δ^* is an effective opening.

What remains to be defined is the shape of the new TSLs $N(\Delta^*)$ and $M(\Delta^*)$, as well as the definition of the effective opening Δ^*. Conditions that should be satisfied are:

- $N = M = 0$ when $\Delta^* \geq \Delta_c$;
- Laws $N(\Delta^*)$ and $M(\Delta^*)$ must be monotonically decreasing;
- Continuity in resultant stresses** between unfractured and fractured stage at $\Delta^* = 0$ should be ensured. This is the case if $N(0) = N_0$ and $M(0) = M_0$, where N_0 et M_0 are respectively the value of $\langle n^{11} \rangle$ and $\langle m^{11} \rangle$ at fractured initialization. These are defined when $\sigma_c = \frac{6|M_0|}{h^2} + \frac{N_0}{h}$;
- At the end of the fracture process, the work induced by the TSLs $\int N(\Delta^*) d([\![u_1]\!]) + \int M(\Delta^*) d([\![-u_{3,1}]\!])$ added to the change of internal energy of the structure should

**It has been demonstrated by K.D. Papoulia *et al.* in [46] that if the continuity is not ensured between unfractured and fractured stages, convergence problems can occur.

correspond to hG_c;

- In case of unloading during the fracture process a linearly decreasing law is used to have $N = M = 0$ in $\Delta^* = 0$ as suggested by G.T. Camacho *et al.* in [3] (see figure 9).

The relations $N(\Delta^*)$ and $M(\Delta^*)$ can be determined experimentally, but in the case of this work a monotonically linearly decreasing law is chosen to illustrate the idea,

$$N(\Delta^*) = \begin{cases} N_0 \left(1 - \frac{\Delta^*}{\Delta_c}\right) \text{ if } \Delta^*_{\max} \leq \Delta^* \leq \Delta_c \\ N_0 \left(\frac{\Delta^*}{\Delta^*_{\max}} - \frac{\Delta^*}{\Delta_c}\right) \text{ if } \Delta^* < \Delta^*_{\max} \\ 0 \text{ if } \Delta^* > \Delta_c \end{cases} \tag{45}$$

$$M(\Delta^*) = \begin{cases} M_0 \left(1 - \frac{\Delta^*}{\Delta_c}\right) \text{ if } \Delta^*_{\max} \leq \Delta^* \leq \Delta_c \\ M_0 \left(\frac{\Delta^*}{\Delta^*_{\max}} - \frac{\Delta^*}{\Delta_c}\right) \text{ if } \Delta^* < \Delta^*_{\max} \\ 0 \text{ if } \Delta^* > \Delta_c \end{cases} \tag{46}$$

$$\tag{47}$$

where $\Delta^*_{\max}$ is the maximal effective opening reached during the simulation.

In order to define the effective opening Δ^* the simple pure traction and pure bending cases are studied. In these cases, the value Δ^* can be determined easily as the energy released must be equal to hG_c. If the beam is in pure tension the energy released is given by,

$$\int_0^{\Delta_c} N(\Delta_x) d\Delta_x = \frac{N_0 \Delta_c}{2} = \frac{2h\sigma_c G_c}{2\sigma_c} = hG_c \tag{48}$$

$$\tag{49}$$

with Δ_x the jump of displacement along x-axis ($[\![u_1]\!]$) and where $N_0 = h\sigma_c$. This shows that in pure tension $\Delta^* = \Delta_x$.

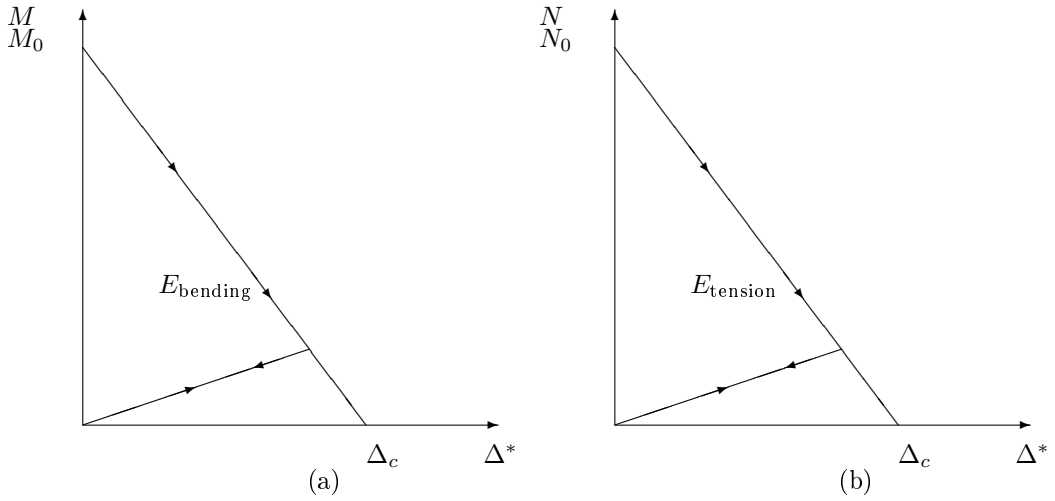

Figure 9. Linearly decreasing monotonic law for (a) resultant bending stress and for (b) resultant membrane stress.

In the case of pure bending this energetic consideration leads to the following choice for the opening,

$$\Delta^* = \frac{h}{6}\Delta_r \tag{50}$$

with Δ_r the opening in rotation given by $[\![-u_{3,1}]\!]$ if the fracture is initialized for positive bending $M_0 > 0$ and by $[\![u_{3,1}]\!]$ if $M_0 < 0$. Indeed,

$$\int_0^{\Delta_{rc}} M(\Delta^*) d\,[\![-u_{3,1}]\!] = \int_0^{\Delta_c} \pm\frac{6}{h} M_0 \left(1 - \frac{\Delta^*}{\Delta_c}\right) d\Delta^* = \frac{6}{h}\frac{h^2\sigma_c}{6}\frac{\Delta_c}{2} = hG_c \tag{51}$$

as $M_0 = \pm\frac{h^2\sigma_c}{6}$ if the fracture is initialized for positive or negative bending respectively.

For combined cases, the value of Δ^* is chosen as a linear combination of the two previous cases,

$$\Delta^* = (1-\beta)\Delta_x + \beta\frac{h}{6}\Delta_r \tag{52}$$

the parameter β has to be equal to zero if the loading is in tension only and equal to 1 for a pure bending problem. This is ensured by choosing β as the ratio at fracture initialization between the bending part of stress and the fracture strength σ_c,

$$\beta = \frac{|6/hM_0|}{N_0 + |6/hM_0|} \tag{53}$$

In case of bending rupture for a beam under tension β will be between 0 and 1, but in case of a beam under compression, fracture can still happen for higher bending stress. In that case β is larger than 1. This definition of Δ^* allows to release an energy quantity equal to hG_c for any coupled loadings.

Nevertheless, as the DG method ensures weakly the continuity, there is an initial jump before fracture and so at fracture's initialization $\Delta_0^* \neq 0$. To guarantee the continuity between pre-fracture and fracture stages, the initial jump at fracture initialization Δ_0^* is subtracted from Δ^*,

$$\Delta_{true}^* = \Delta^* - \Delta_0^* \tag{54}$$

Finally, the use of relations (23) and (44) leads to the new weak formulation of the problem

$$\begin{aligned}
&\sum_n \int_{l_e} \left[n^{11}\delta u_{1,1} + m^{11}\delta(-u_{3,11}) \right] dx \\
&+ \sum_s \left\{ (1-\alpha_s) \left(\langle n^{11} \rangle [\![\delta u_1]\!] + \langle Eh\delta u_{1,1} \rangle [\![u_1]\!] + [\![u_1]\!] \left\langle \frac{\beta_2 Eh}{h_s} \right\rangle [\![\delta u_1]\!] \right.\right. \\
&\left. + \langle m^{11} \rangle [\![\delta(-u_{3,1})]\!] + \left\langle \frac{Eh^3}{12}\delta(-u_{3,11}) \right\rangle [\![-u_{3,1}]\!] + [\![-u_{3,1}]\!] \left\langle \frac{\beta_1 Eh^3}{12h_s} \right\rangle [\![-\delta u_{3,1}]\!] \right) \\
&\left. + \gamma_s [\![\delta u_3]\!] \left\langle \frac{\beta_3 Eh}{2(1+\nu)h_s} \right\rangle [\![\delta u_3]\!] \right\} \\
&+ \sum_s \alpha_s \left(N(\Delta_{true}^*)\delta [\![u_1]\!] + M(\Delta_{true}^*)\delta [\![-u_{3,1}]\!] \right) = 0
\end{aligned} \tag{55}$$

where γ_s is equal to 1 if $\alpha_s = 0$ or if $\alpha_s = 1$ and $\Delta_{true}^* < \Delta_c$. This DG terms has to be kept until the end of fracture as the shearing has to be constrained even during the fracture.

	DCB
material properties	
Young's modulus (E)	71 [GPa]
Poisson's coefficient (ν)	0.21 [-]
fracture strength (σ_c)	400 [MPa]
energy strength (G_c)	8800 [J/m^2]

Table II. Material properties of the clamped beam

4.2. Numerical example: Double Clamped Beam

To demonstrate the ability of the presented framework to model fracture phenomena, studies are made on a double clamped beam, whose material properties are given in table II. The beam is firstly loaded only in bending before the realization of simulations in with combined tension-bending loadings. For all the following tests, the beam is discretized with 16 full DG cubic elements, so there are 128 degrees of freedom in the model, and the parameters β_1, β_2 and β_3 are respectively fixed to 10, 10 and 1000.

4.2.1. Pure bending fracture test This test case, represented in Figure 10, consists in a vertical displacement applied downward at the middle of the beam. This introduces a vertical displacement field symmetric with respect to the center of the beam describing by [43]

$$u_z(x) = 4\frac{x^2(3L-4x)}{L^3}u_z(\frac{L}{2})\ x \in [0, L/2] \tag{56}$$

where $u_z(\frac{L}{2})$ is the applied vertical displacement. Stress is maximal at clamping (in upper skin of beam) and at the middle of the beam (in lower skin of it). This maximal value is given by,

$$\sigma_{\max} = \frac{12Eh}{L^2}u_z(\frac{L}{2}) \tag{57}$$

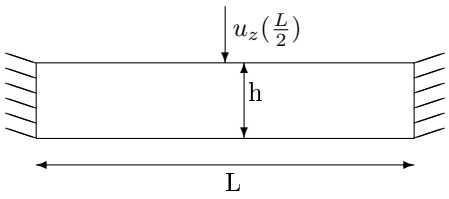

Figure 10. Representation of a double clamped beam in bending

In this example, fracture at clamping is not allowed so it will be localized at the center of the beam. After rupture, the double clamped beam (DCB) of length L becomes two simply clamped beams (SCB) of length $L/2$. Note that in the simulation the vertical displacement is applied on both nodes of beam's center. Consequently, the archived force in the not-fractured case is equal to half the force corresponding to the prescribed displacement and the energies compute numerically will have to account for this.

The energy release rate G occurring during the transition can be computed by,

$$G = W_{\text{ext}} - E_{\text{int}} \tag{58}$$

where in this last equation W_{ext} is the work of external forces until complete fracture of the beam, and E_{int} is the internal energy of the beam, see Figure 11. In the following simulations the relation force-displacement is archived and the different area of figure 11 are computed

numerically at the end of simulation. Furthermore, the fracture energy hG_c can be computed by,

$$hG_c = W_{\text{ext, after fracture}} - E_{\text{int, after fracture}} \tag{59}$$

Another useful quantity is the difference of internal energy (ΔE_{int}) between the fractured and unfractured cases. Indeed this quantity can be used to predict if there is a need for external energy to achieve a complete rupture on the beam thickness. If $\Delta E_{\text{int}} > hG_c$, once the crack is detected, the unique solution of the problem is a complete rupture of the beam, while, on the contrary if $\Delta E_{\text{int}} < hG_c$, energy from the loading, and thus a further displacement increment, is required in order to achieve complete rupture. ΔE_{int} can be computed analytically, leading to

$$\Delta E_{\text{int, bend}} = \frac{hL_{DCB}}{24E}\sigma^2_{c,\text{ bending}} \tag{60}$$

where $\sigma_{c,\text{ bending}}$ is the bending stress reached when fracture is initiated.

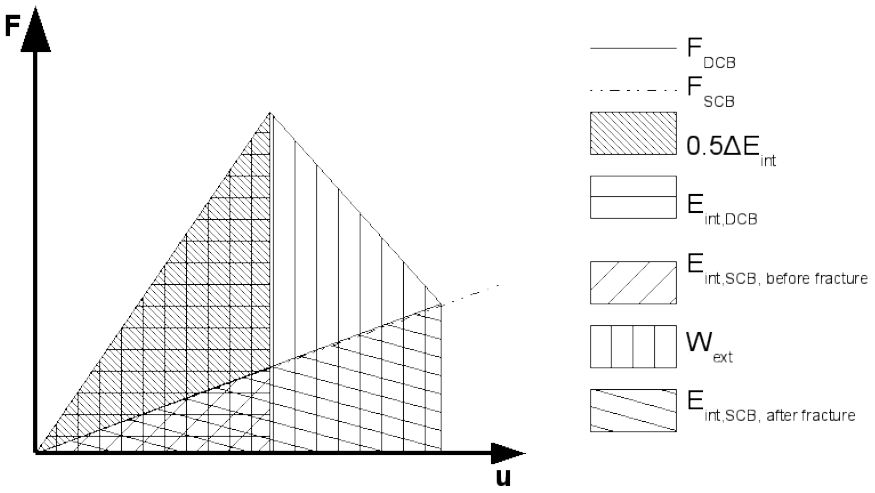

Figure 11. Force-Displacement relation of DCB (half beam) and SCB

This simulation is performed first for a beams of 200 mm in length and 20 mm in height. $\Delta E_{\text{int, bend}}$ computed thanks to equation (60) is equal to $375.58[J]$ while the fracture energy is equal to $0.02 * G_c = 176[J]$. As $\Delta E_{int,bend}$ is larger than twice the fracture energy, the fracture happens in one increment of displacement as illustrated on figure 12. Picture (a) of this figure plots the maximal stress at center of the beam in terms of the prescribed displacement. The stress increases until it reaches the value of the fracture strength (400 MPa). It then falls down to zero as the center of the DCB becomes a free extremity of a SCB. Picture (b) gives the relation between the force and the prescribed displacement at the middle of the DCB. This curve is in agreement with the picture (a) as the force follows the analytical value of a DCB and a SCB respectively before and after the fracture. Moreover $\Delta E_{\text{int, bend}}$ can be computed by numerical integration of this curve. The calculation gives a result of 381.47 [J], which is very close of the analytical value. Pictures (c) and (d) represent the deformation's map respectively before and after fracture. Again before fracture the deformation's map is the one of a DCB and after fracture, it is the one of two SCB. Finally, picture (e) depicts the relation between the angle $u_{3,1}$ at middle of the DCB vs the prescribed displacement. This picture shows that before fracture the angle is equal to zero and it is equal to the analytical value of a SCB after fracture.

Another simulation is realized on a DCB with a length of 50 mm and a height of 2.5 mm. For this DCB the application of formula (60) yields $\Delta E_{\text{int, bend}} = 11.737[J]$. As $\Delta E_{\text{int, bend}}$ is lower than the fracture energy of $22[J]$ for this DCB, there is a fracture process. This process is illustrated on the pictures of figure 13. Picture (a) of this figure depicts the maximal stress at the middle of the beam. As for the previous case there is fracture when the stress reaches the fracture strength but, this time, the stress decreases linearly with the prescribed displacement.

The same conclusion is valid for the force-displacement relation plotted on picture (b). This picture shows that after fracture the force decreases linearly with the displacement until it reaches the curve force-displacement of a SCB. The numerical integration gives a value of $12.33[J]$ for $\Delta E_{\text{int, bend}}$ which is in accordance with it analytical value. Moreover, the use of equation (58) yields an energy released equal to $21.98[J]$, which is very close to its analytical value. Pictures (c) and (d) show, as for the previous case, that the displacement field is equal before and after fracture to the displacement field of a DCB and of a SCB respectively. Finally picture (e) depicts the value of the angle $u_{3,1}$ in function of the prescribed displacement. As for the stress and force fields, the value of $u_{3,1}$ increases linearly after fracture initialization to reach at the end of fracture process the analytical value of a SCB.

4.2.2. Combined tension-bending fracture test In order to demonstrate that the model of fracture presented releases the right amount of energy for any loading conditions, a test involving combined tension and bending is presented. The test is the same as previous excepted that a constant x-displacement is added (see figure 14). The simulations are performed on a DCB of 50 mm in length and 2.5 mm in height.

The characteristic quantity ΔE_{int} has now to consider the internal energy in tension, which gives the relation,

$$\Delta E_{int} = \frac{hL_{DCB}}{2E}\left(\frac{13}{12}\beta^2 - 2\beta + 1\right)\sigma_c^2 \tag{61}$$

where β is the coupling parameter (53). The force-displacement relation depicted on figure 11, illustrates now the energy released in bending ($E_{\text{int, bend}}$). The total released energy is obtained after adding to $E_{\text{int,bend}}$ the energy released in tension ($E_{int,tens}$).This last contribution is given

by,

$$E_{\text{int, tens}} = \frac{1}{2} N_0 \Delta_{xc} \tag{62}$$

where Δ_{xc} is the value of Δ_x when $\Delta^*_{true} = \Delta_c$. This energy can also be determined analytically by,

$$E_{\text{int, tens}} = \frac{Eh}{2L} u^2_{x,\text{ pres}} \tag{63}$$

as there is no work of external forces in tension.

The energies obtain for different loading conditions are collected in table III. This table shows that the total energy released (E_{released}) is equal to the fracture energy for any $u_{x,pres}$, the small differences being due to the application of the prescribed displacements by steps. For $u_{x,\text{ pres}} = 10e^{-5}$, the difference of internal energy between unfractured and fractured case is larger than $hG_c = 22$ [J]. Therefore for this prescribed displacement the fracture occurs in one increment of displacement and the computation of the energies released in tension and in bending is meaningless. Furthermore the simulation is performed for a negative $u_{x,\text{ pres}} = -2e^{-5}$ to show that the method remains valid in the compression case. As no contact is taken into account during the simulation an energy quantity equal to $E_{\text{int, tens}}$ is released in compression and so the energetic balance is exactly the same as for $u_{x,\text{ pres}} = 2e^{-5}$. The difference between the 2 cases is the value of the prescribed u_z leading to fracture (see figure 15), which explains the difference of ΔE_{int} between the 2 simulations.

Figure 15 illustrates the results for the different prescribed displacements. Picture (a) depicts the maximal stress at the center of the DCB and shows that for every value of the prescribed displacement the fracture begins when the stress reaches the value of σ_c. Picture (b) represents the relation force-displacement in the z-direction. It can be seen that as $u_{x,\text{ pres}}$ increases the

$u_{x,pres}$	β	ΔE_{int}	$E_{\text{int, bend}}$	$E_{\text{int, tens}}$	E_{released}
$-2e^{-5}$	1.0692	14.8043	21.26	0.71	21.98
0	1	12.33	21.98	0	21.98
$2e^{-5}$	0.93	11.39	21.26	0.71	21.98
$4e^{-5}$	0.86	11.99	19.14	2.84	21.98
$6e^{-5}$	0.79	14.11	15.59	6.39	21.98
$8e^{-5}$	0.72	17.76	10.63	11.36	21.99
$10e^{-5}$	0.66	22.95	–	–	–

Table III. Double Clamped Beam with combined loadings: Values of different energetic quantities for different prescribed x-displacement

value of the z-force decreases and the complete fracture happens for a lower value of u_z. This result is consistent with the fact than when $u_{x,\text{ pres}}$ increases the bending part of the stress is lower at fracture initialization, which implies a lower resultant bending stress at fracture initialization (see picture (c)) and therefore a lower z-force. Finally pictures (c) and (d) represent respectively the relation $M(\Delta_r)$ and $N(\Delta_x)$. These graphs show that when $u_{x,\text{ pres}}$ increases both the resultant stress at fracture initialization N_0 and the value of Δ_x reached at the end of the fracture process increase, which is physically explained due to the fact that there is more energy to be released in tension.

5. CONCLUSIONS

In this article a new full-DG formulation of Euler Bernoulli beams is presented and the numerical properties of this method are studied. It is shown (theoretically and numerically)

that the suggested formulation has the same numerical properties of consistency and convergence rate in the $\boldsymbol{L}^2$ norm than other finite elements formulation. Moreover it is set out that the present framework gives the same results as the CG/DG formulation of problem previously introduced by G. Engel *et al.* in [40].

The main interest of the full-DG formulation is its ability of being easily coupled with cohesive zone models. Indeed as interface elements are introduced from the beginning, cohesive elements can be inserted very easily and a new cohesive zone model based on resultant stresses is inserted in the presented formulation. Tests on a double clamped beam are simulated with success, which proves the interest of the method.

This article constitutes an exploration of the full-DG framework for thin structures. In further works the method will be extended to shells, which will allow to simulate more complex problems.

REFERENCES

1. D. S. Dugdale. Yielding of steel sheets containing slits. *Journal of the Mechanics and Physics of Solids*, 8(2):100–104, May 1960.
2. G.I. Barenblatt. The mathematical theory of equilibrium cracks in brittle fracture. volume Volume 7, pages 55–129. Elsevier, 1962.
3. G. T. Camacho and M. Ortiz. Computational modelling of impact damage in brittle materials. *International Journal of Solids and Structures*, 33(20-22):2899–2938, 1996.
4. Majid Anvari, Jun Liu, and Christian Thaulow. Dynamic ductile fracture in aluminum round bars: experiments and simulations. *International Journal of Fracture*, 143(4):317–332, 2007.
5. Pedro M. A. Areias, J. H. Song, and Ted Belytschko. Analysis of fracture in thin shells by overlapping paired elements. *Computer Methods in Applied Mechanics and Engineering*, 195(41-43):5343–5360, 2006.
6. Fehmi Cirak, Michael Ortiz, and Anna Pandolfi. A cohesive approach to thin-shell fracture and fragmentation. *Computer Methods in Applied Mechanics and Engineering*, 194(21-24):2604–2618, 2005.

7. R. Raghupathy A. Rusinek F. Zhou J. F. Molinari, G. Gazonas. The cohesive element approach to dynamic fragmentation: the question of energy convergence. *International Journal for Numerical Methods in Engineering*, 69(3):484–503, 2007.
8. A. Pandolfi, P. Krysl, and M. Ortiz. Finite element simulation of ring expansion and fragmentation: The capturing of length and time scales through cohesive models of fracture. *International Journal of Fracture*, 95(1):279–297, 1999.
9. I. Scheider and W. Brocks. Simulation of cup-cone fracture using the cohesive model. *Engineering Fracture Mechanics*, 70(14):1943–1961, 2003.
10. Randolph R. Settgast and Mark M. Rashid. Continuum coupled cohesive zone elements for analysis of fracture in solid bodies. *Engineering Fracture Mechanics*, In Press, Corrected Proof:–, –.
11. Viggo Tvergaard. Crack growth predictions by cohesive zone model for ductile fracture. *Journal of the Mechanics and Physics of Solids*, 49(9):2191–2207, 2001.
12. P. A. Klein, J. W. Foulk, E. P. Chen, S. A. Wimmer, and H. J. Gao. Physics-based modeling of brittle fracture: cohesive formulations and the application of meshfree methods. *Theoretical and Applied Fracture Mechanics*, 37(1-3):99–166, December 2001.
13. W Celes. A compact adjacencybased topological data structure for finite element mesh representation. *International journal for numerical methods in engineering*, 64(11):1529–, 2005.
14. Zhengyu (Jenny) Zhang, Glaucio H. Paulino, and Waldemar Celes. Extrinsic cohesive modelling of dynamic fracture and microbranching instability in brittle materials. *International Journal for Numerical Methods in Engineering*, 72(8):893–923, 2007.
15. Alejandro Mota, Jaroslaw Knap, and Michael Ortiz. Fracture and fragmentation of simplicial finite element meshes using graphs. *International Journal for Numerical Methods in Engineering*, 73(11):1547–1570, 2008.
16. Isaac Dooley, Sandhya Mangala, Laxmikant Kale, and Philippe Geubelle. Parallel simulations of dynamic fracture using extrinsic cohesive elements. *J. Sci. Comput.*, 39(1):144–165, 2009.
17. F. Perales, S. Bourgeois, A. Chrysochoos, and Y. Monerie. Two field multibody method for periodic homogenization in fracture mechanics of nonlinear heterogeneous materials. *Engineering Fracture Mechanics*, 75(11):3378–3398, July 2008.
18. Vincent Acary, Yann Monerie, V. Acary, Y. Monerie, and Acary V. et al. Nonsmooth fracture dynamics using a cohesive zone approach. Technical report, INRIA, 2006.
19. Hill T.R. Reed W.H. Triangular mesh methods for the neutron transport equation. In *Conference:*

National topical meeting on mathematical models and computational techniques for analysis of nuclear systems, Ann Arbor, Michigan, USA, 8 Apr 1973; Other Information: Orig. Receipt Date: 31-DEC-73, 1973.

20. Douglas N. Arnold, Franco Brezzi, Bernardo Cockburn, and L. Donatella Marini. Unified analysis of discontinuous galerkin methods for elliptic problems. *SIAM Journal on Numerical Analysis*, 39(5):1749–1779, 2002.
21. P. Hansbo and M. G. Larson. A discontinuous galerkin method for the plate equation. *Calcolo*, 39(1):41–59, 2002.
22. D. Sulsky A. Lew, P. Neff and M. Ortiz. Optimal bv estimates for a discontinuous galerkin method for linear elasticity. *Appl Math Res Express*, 2004(3):73–106, 2004.
23. Fatih Celiker, Bernardo Cockburn, and Henryk K. Stolarski. Locking-free optimal discontinuous galerkin methods for timoshenko beams. *SIAM Journal on Numerical Analysis*, 44(6):2297–2325, 2006.
24. S. Guzey, H. K. Stolarski, B. Cockburn, and K. K. Tamma. Design and development of a discontinuous galerkin method for shells. *Computer Methods in Applied Mechanics and Engineering*, 195(25-28):3528–3548, 2006.
25. R. Radovitzky L. Noels. A general discontinuous galerkin method for finite hyperelasticity. formulation and numerical applications. *International Journal for Numerical Methods in Engineering*, 68(1):64–97, 2006.
26. A. Lew A. Ten Eyck. Discontinuous galerkin methods for non-linear elasticity. *International Journal for Numerical Methods in Engineering*, 67(9):1204–1243, 2006.
27. H. K. Stolarski S. Guzey, B. Cockburn. The embedded discontinuous galerkin method: application to linear shell problems. *International Journal for Numerical Methods in Engineering*, 70(7):757–790, 2007.
28. L. Noels and R. Radovitzky. Alternative approaches for the derivation of discontinuous galerkin methods for nonlinear mechanics. *J. Appl. Mech.*, 74(5):1031–1036, September 2007.
29. N. Tien Dung G. N. Wells. A c0 discontinuous galerkin formulation for kirchhoff plates. *Computer Methods in Applied Mechanics and Engineering*, 196(35-36):3370–3380, 2007.
30. R. Rangarajan A. Lew, A. Eyck. Some applications of discontinuous galerkin methods in solid mechanics. *IUTAM Symposium on Theoretical, Computational and Modelling Aspects of Inelastic Media*, pages 227–236, 2008.
31. A. Lew A. Eyck, F. Celiker. Adaptive stabilization of discontinuous galerkin methods for nonlinear elasticity: Motivation, formulation, and numerical examples. *Computer Methods in Applied Mechanics*

and Engineering, 197(45-48):3605–3622, August 2008.

32. R. Radovitzky L. Noels. An explicit discontinuous galerkin method for non-linear solid dynamics: Formulation, parallel implementation and scalability properties. *International Journal for Numerical Methods in Engineering*, 74(9):1393–1420, 2008.
33. L. Noels and R. Radovitzky. A new discontinuous galerkin method for kirchhoff-love shells. *Computer Methods in Applied Mechanics and Engineering*, 197(33-40):2901–2929, 2008.
34. L. Noels. A discontinuous galerkin formulation of non-linear kirchhoff-love shells. *International Journal for Numerical Methods in Engineering*, 78(3):296–323, 2009.
35. Yongxing Shen and Adrian Lew. An optimally convergent discontinuous galerkin-based extended finite element method for fracture mechanics. *International Journal for Numerical Methods in Engineering*, 9999(9999):n/a, 2009.
36. J. Mergheim, E. Kuhl, and P. Steinmann. A hybrid discontinuous galerkin/interface method for the computational modelling of failure. *Communications in Numerical Methods in Engineering*, 20(7):511–519, 2004.
37. R. Radovitzky, A. Seagraves, M. Tupek, and L. Noels. A hybrid dg/cohesive method for modeling dynamic fracture of brittle solids. Submitted to Computer Methods in Applied Mechanics and Engineering, –.
38. A. Seagraves and R. Radovitzky. *Advances in Cohesive Zone Modeling of Dynamic Fracture, Dynamic Failure of Materials and Structures.* Springer Science and Business Media, –.
39. R. Abedi, M. Hawker, R. Haber, and K. Matous. An adaptive spacetime discontinuous galerkin method for cohesive models of elastodynamic fracture. *International Journal for Numerical Methods in Engineering*, 81(10):1207–1241, 2010.
40. G. Engel, K. Garikipati, T. J. R. Hughes, M. G. Larson, L. Mazzei, and R. L. Taylor. Continuous/discontinuous finite element approximations of fourth-order elliptic problems in structural and continuum mechanics with applications to thin beams and plates, and strain gradient elasticity. *Computer Methods in Applied Mechanics and Engineering*, 191(34):3669–3750, July 2002.
41. J. C. Simo and D. D. Fox. On stress resultant geometrically exact shell model. part i: formulation and optimal parametrization. *Comput. Methods Appl. Mech. Eng.*, 72(3):267–304, 1989.
42. J. C. Simo, D. D. Fox, and M. S. Rifai. On a stress resultant geometrically exact shell model. part ii: the linear theory; computational aspects. *Comput. Methods Appl. Mech. Eng.*, 73(1):53–92, 1989.
43. S. Cescotto C. Massonnet. *Mecanique des materiaux.* De Boeck, 3 edition, 1994.
44. J.R. Rice. *Mathematical analysis in the mechanics of fracture*, volume 2. IN H. Liebotwitz, 1968.

45. A. A. Griffith. The phenomena of rupture and flow in solids. *Philosophical Transactions of the Royal Society of London. Series A, Containing Papers of a Mathematical or Physical Character*, 221:163–198, 1921.

46. Katerina D. Papoulia, Chin-Hang Sam, and Stephen A. Vavasis. Time continuity in cohesive finite element modeling. *International Journal for Numerical Methods in Engineering*, 58(5):679–701, 2003.

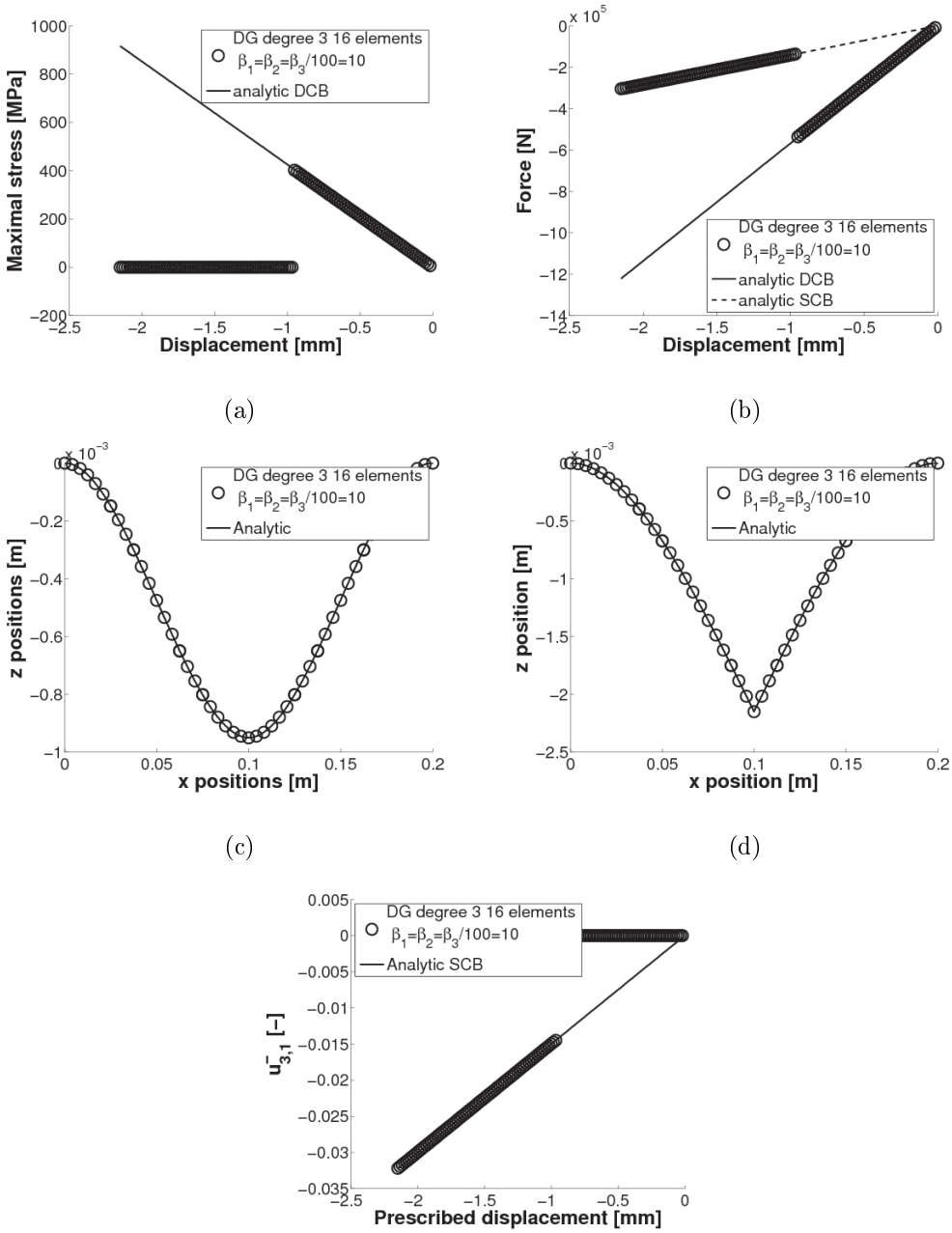

Figure 12. Double clamped beam in quasi-static bending ($L = 200$ mm, $h = 20$ mm) (a) maximal stress at beam's center, (b) force-displacement relation, displacement field (c) at fracture initialization and (d) after fracture and (e) angle $u_{3,1}$ at center of DCB

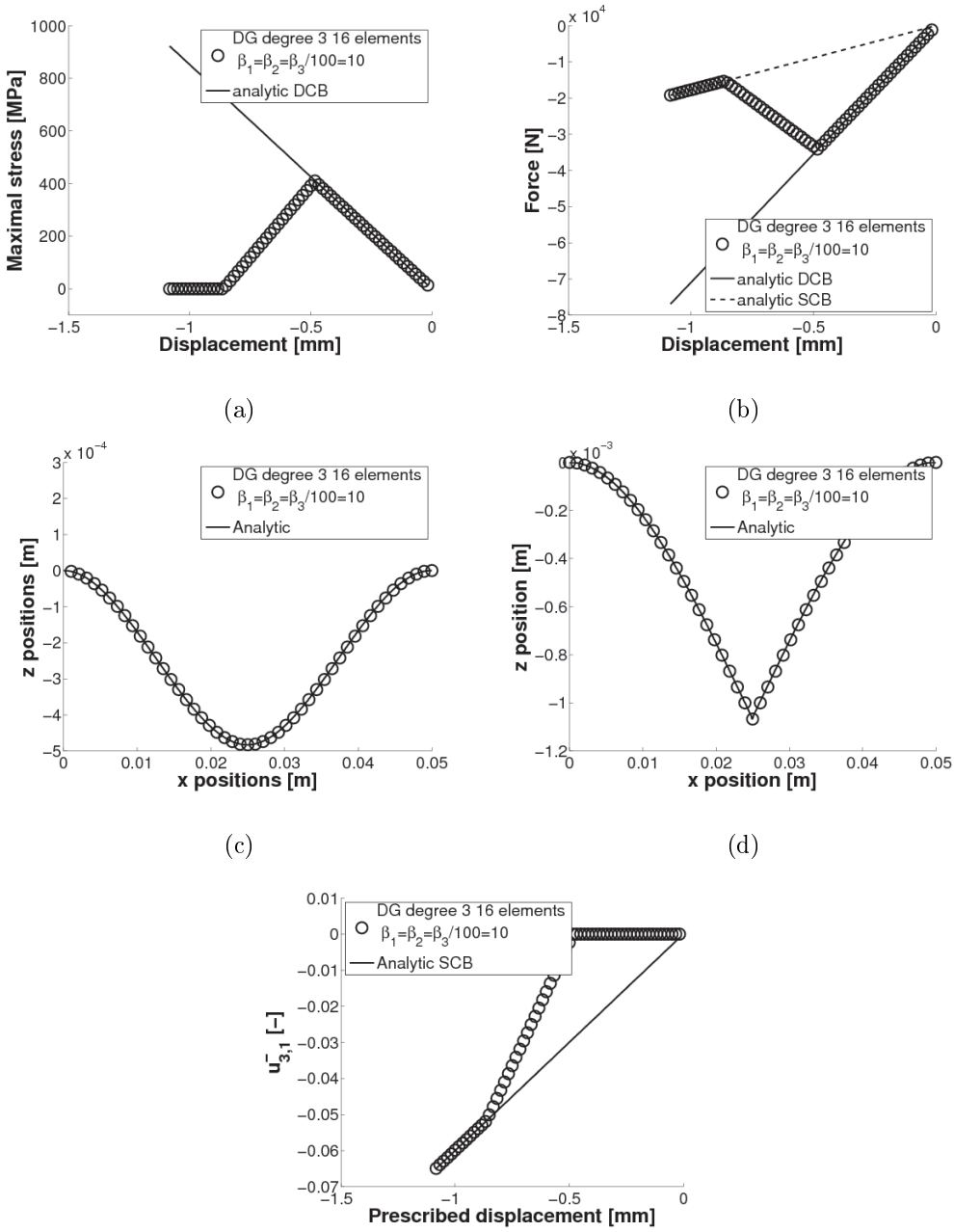

Figure 13. Double clamped beam in quasi-static bending ($L = 50$ mm, $h = 2.5$ mm) (a) maximal stress at beam's center, (b) force-displacement relation, displacement field at fracture initialization (c) and (d) after fracture and (e) angle $u_{3,1}$ at center of DCB.

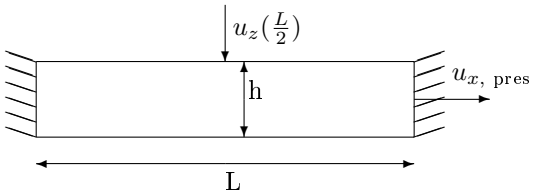

Figure 14. Representation of a double clamped beam in combined case

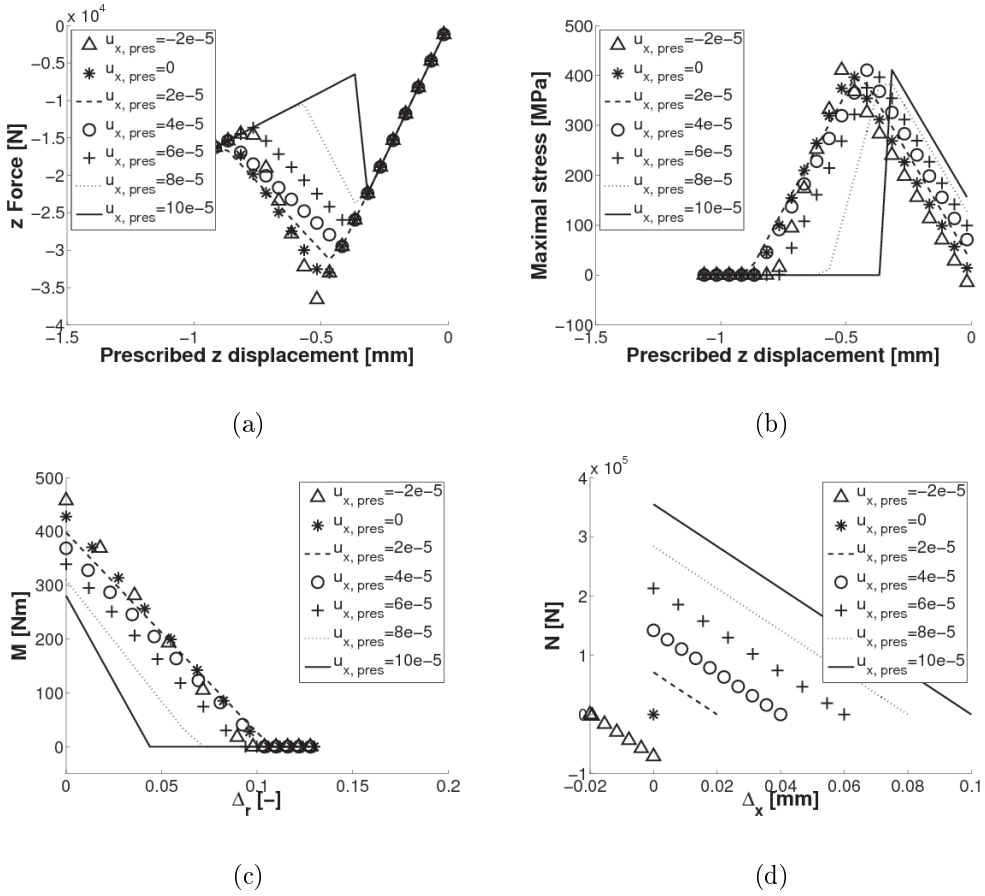

(a) (b)

(c) (d)

Figure 15. Double Clamped Beam with combined loadings for different prescribed x-displacements: (a) maximal stress at center of DCB with respect to the z-displacement, (b) z-Force vs z-displacement, (c) relation $M(\Delta_r)$ and (d) relation $N(\Delta_x)$